

THESIS FOR THE DEGREE OF
LICENTIATE OF ENGINEERING

in

Thermo and Fluid Dynamics

**On the numerical modelling of impinging jets
heat transfer**

MIRKO BOVO

Department of Applied Mechanics
CHALMERS UNIVERSITY OF TECHNOLOGY
Gothenburg, Sweden, 2011

On the numerical modelling of impinging jets heat transfer

MIRKO BOVO

© MIRKO BOVO, 2011

THESIS FOR LICENTIATE OF ENGINEERING no 2011:04

ISSN 1652-8565

Department of Applied Mechanics

Chalmers University of Technology

SE-412 96 Gothenburg

Sweden

Telephone +46 (0)31 772 1000

Chalmers Reproservice

Gothenburg, Sweden 2011

On the numerical modelling of impinging jets heat transfer

MIRKO BOVO

Division of Combustion

Department of Applied Mechanics

CHALMERS UNIVERSITY OF TECHNOLOGY

Gothenburg, Sweden 2011

Abstract

This thesis collects two studies on heat transfer in impinging jets and on methods for modelling flows of this kind using CFD. Stationary impinging jets with different nozzle-to-wall distances ($z/D = 2$ and 6) and Re (10000, 20000, 23000, 30000) are modelled. Steady-state models capture the important features of heat transfer in these jets. The inlet velocity profile plays an important role on the results. The $k-\varepsilon$ and $k-\omega$ turbulence models do not offer adequate performance. However, the V2F model generates useful results even with low-order discretization schemes. The effects of varying the mesh density and topology also studied, and the computational cost of different model set-ups is compared. Transient simulations were shown to be useful for studying the dynamics of turbulent flow in the impinging jet shear layer. Simulations are performed using the LES model, which resolves the turbulent fluctuations, and with the DES, V2F, and $k-\varepsilon$ turbulence models, which do not; a number of parameters are varied during the testing of the LES model. The effects of inlet turbulence were studied by superimposing synthetic turbulent fluctuations at the inlet. The LES, DES and V2F models are shown to capture the time-average heat transfer coefficient in a fashion that agreed well with the available experimental data.

Acknowledgements

I would like to express my sincere gratitude to Volvo Car Corporation, Chalmers University of Technology and the Swedish authorities for supporting my PhD project.

I would also like to thank various people who helped me in my work. I am very grateful to my supervisor, Lars Davidson for many interesting discussions in which he shared his deep knowledge with me. Without the assistance of Sassan Etemad, I would probably not even have been able to get started with my research. I am also indebted to Ingemar Denbratt, Peter Norin, Anders Thorell, and Börje Grandin for believing in me and my project. I am very grateful also to Mattias Ljungqvist, Joop Somhorst, my group at Volvo Car Corporation and my colleagues at Chalmers.

Elin and Giovanni helped me to survive the Swedish winter and to enjoy the Swedish summer, and I am grateful to Mamma, Papa', Laura e Daniele for giving me so much love from so far away.

Finally, I am very grateful to the people of Sweden because, better than most other countries, they create with their culture the playground for success for many like me willing to do good.

Background

The increasing demand for energy-efficient vehicles drives the development of more effective internal combustion engines (ICE). This demand is the combined result of economic and environmental concerns. The price of fuels is rapidly growing following the elementary economic law of supply and demand. Consequently, there is increasing interest in engines capable of efficiently converting the chemical energy of fuel into useful work. Efficient engines are, in general, also more environmentally friendly. Indeed, reductions in fuel consumption correlate directly with reductions in the emissions of CO₂ which is associated with global warming. Although absolute reductions in emissions would be beneficial to the environment, engines with high efficiency might cause a different source of pollution. For example, the use of high combustion temperatures increases the efficiency but also favors the formation of NO_x (nitrogen oxides), which are “greenhouse gasses”. Clearly, it is necessary to identify an optimal tradeoff between efficiency and emissions that minimizes the environmental impact of the ICE.

Heat losses through the walls of the combustion chamber are a major player in the total energy balance of an ICE. Hence, even a small reduction of these losses has a direct and beneficial effect on the engine efficiency. Furthermore, heat losses are directly related to the in-cylinder temperature, which is a key variable in determining two important properties of the engine: its emissions profile and its durability. The combustion process in ICE is strongly influenced by the local temperature. The relative contribution to engine emission due to near wall temperature gradients is becoming increasingly important in the absolute level of pollutant emission. Engines specific power is increasing to satisfy the market request for high performance and good fuel economy. This process is often referred to as “downsizing”. However, increases in specific power also increase the thermal load on engine components. Thermal stresses play an important role in mechanical failure, specifically, they are the main responsible for the low frequency fatigue¹.

Heat transfer (and thus heat loss) is driven by temperature difference. The temperature in the combustion chamber is, on average, much higher than that of the surrounding walls². The transfer of heat between a solid and a fluid is also strongly affected by the heat transfer coefficient. This fictitious parameter combines together the fluid and the flow properties associated to the heat transfer phenomenon. The heat transfer coefficient allows expressing the heat transfer in the following simple expression:

$$\textit{Specific heat flux} = \textit{Heat transfer coefficient} \cdot \textit{Temperature difference}$$

¹ Low frequency fatigue is a periodic stress associated with engine warm-up and cool-down. High frequency fatigue is associated with the high pressure during the compression-power stroke.

² During intake stroke the fresh charge is in general cooler than the combustion chamber walls.

From the expression above, it follows that the greatest heat losses occur when and where the combination of heat transfer coefficient and temperature is highest. This occurs during the end of the compression and the beginning of the power stroke. At this stage, the combustion process is proceeding at its maximum rate, occurring at high pressure and density and with high levels of turbulence intensity. In this phase of the engine cycle the piston is close to top dead center, position which minimizes the surface area exposed to the hot gases. This limits heat losses but means that the small exposed surface experiences very high specific heat fluxes.

The heat transfer phenomena occurring during the combustion event can be studied in detail. The combustion process in direct injection compression ignition engines such as modern diesel engines has been studied in detail for a long time. One specific aspect of this process plays a major role in the generation of localized regions with high levels of heat transfer: impinging jets. During the power cycle, highly pressurized liquid fuel is injected into the combustion chamber through a nozzle. The fuel enters the environment with high momentum and travels towards the chamber wall. The friction due to the high velocity brakes up the fuel into small droplets which evaporate in contact with the high temperature compressed air. Eventually the vapor self-ignites, initiating beginning the combustion. The vaporized fuel continues to move towards the combustion chamber wall with a reduced velocity but dragging also air with it. This moving, reacting flow generates a jet-like flame that impinges on the wall. Impinging jets generate very high levels of heat transfer coefficient in the impingement zone. A consequence of this phenomenon is a localized high temperature spot on the combustion chamber wall that increases the likelihood of mechanical failure.

Modern processes for the design of modern design process of ICE are highly reliant on numerical simulation. This technique is already well established, but continues to be refined and to find new areas of application. Its growth is largely due to ongoing improvements in computer technology improvement, which make it possible to solve ever-larger models in reasonable timeframes. Another important contributor to this growth is the development of new sub-models, such as turbulence models or combustion models capable of more accurately predicting the outcome of a given physical process. The following aphorism provides an interesting perspective on physical modelling:

“If measuring is knowing, then modelling is understanding”

Author unknown

Indeed, it is possible to model a physical phenomenon only to the extent that it is understood. As such, it is important to study phenomena in order to better understand them and to increase the scope for modelling their behavior.

This thesis collects data from two works whose objective was to identify new and improved methods for modelling impinging jets. Specifically, it discusses studies on the steady-state and transient modelling of stationary impinging jets. A number of different simulations were designed, performed, and evaluated by comparison to experimental data.

REPORT

On the transient numerical modelling of impinging jets heat transfer

Abstract

This work compares a number of CFD transient models of an impinging jet. The specific case considered is an impinging jet with $z/D = 6$ and $Re = 23000$. The variables tested are: Turbulence model (LES, $k-\epsilon$, V2F and DES), discretization schemes, mesh density and topology and influence of inlet turbulence for a total of 15 simulations. The comparison is based on the heat transfer prediction compared with experiments, resolved and modelled turbulent kinetic energy upstream of the impingement wall and the computational cost. It is found that the turbulence created in the shear layer plays a stronger role than the inlet turbulence. The LES model reproduces the behavior of turbulent structures with a useful degree of accuracy; the LES, DES and V2F models are capable of accurately predicting heat transfer to the impingement wall.

Key words: impinging jet, heat transfer, CFD, LES, V2F.

Abbreviations

μ molecular viscosity ($\text{kg}/\text{m}^2\text{s}$)

μ_t turbulent viscosity ($\text{kg}/\text{m}^2\text{s}$)

const: constant

D: diameter (m)

h heat transfer coefficient ($\text{W}/\text{m}^2\text{K}$)

k thermal conductivity (W/mK)

k: (specific) turbulent kinetic energy (m^2/s^2)

l turbulent length scale (m)

Nu Nusselt number

r: radius (m)

Re Reynolds number

U, V, W: average velocity (m/s)

u, v, w: velocity (m/s)

u' , v' , w' : velocity fluctuation (m/s)

W_b : bulk inlet velocity (m/s)

y^+ dimensionless wall distance

z: height (m)

ε turbulence dissipation rate (m^2/s^3)

θ : angle (rad or deg)

CFD Computational Fluid Dynamics

CPU Central Processing Unit

DES Detached Eddy Simulation

ICE internal combustion engine

LES Large Eddy Simulation

RANS Reynolds Averaged Navier-Stokes

rms root mean squared

Table of contents

1	Introduction.....	5
2	Impinging jet physics.....	7
2.1	Impinging jet flow features	7
2.2	Impinging jet heat transfer	9
3	Modelling of impinging jets.....	13
3.1	Modelling methodology	13
3.2	Turbulence modelling	16
4	Transient modelling results and discussion	19
4.1	Experimental reference	19
4.2	Simulation results.....	19
4.3	Results from LES simulations.....	20
4.4	Heat transfer, comparison between LES, DES, k- ϵ and V2F.....	27
4.5	Computational cost.....	29
5	Conclusions.....	31
	References.....	33
6	Appendix: Turbulence models description	35
6.1	Standard k- ϵ	35
6.2	V2F model.....	36
6.3	LES.....	37
6.4	DES with standard k- ϵ	37



1 Introduction

Impinging jets flows have remarkable features and find many applications in industry. Consequently, this type of flow has been object of interest for many researchers. However, part of the physics governing impinging jet flows is not fully understood and this prevents a satisfying prediction of the effects of an arbitrary jet configuration.

A particularly interesting aspect of impinging jets is the heat transfer occurring between the fluid and the wall. The convective phenomena give rise to the highest levels of heat transfer coefficient known for single phase flows. Moreover, the heat transfer is strongly dependent on the position relative to the stagnation point. Consequently, the temperature field in the flow and on the wall surface is strongly dependent on the jet's characteristics.

The impinging jet-like flow in ICE (Internal Combustion Engine) combustion chamber is an unwanted bi-effect of the fuel injection / combustion process. The free jet generated during injection increases turbulence and entrainment between air and fuel: these are positive characteristics improving the combustion process. On the other hand, in the near-wall region the impinging jet causes high heat transfer coefficients increasing thermal losses. Moreover, the highly localized heat transfer results in high temperature gradients in the combustion chamber walls and in consequent high thermal induced mechanical stresses. For these reasons it is interesting to study impinging jets on ICE applications.

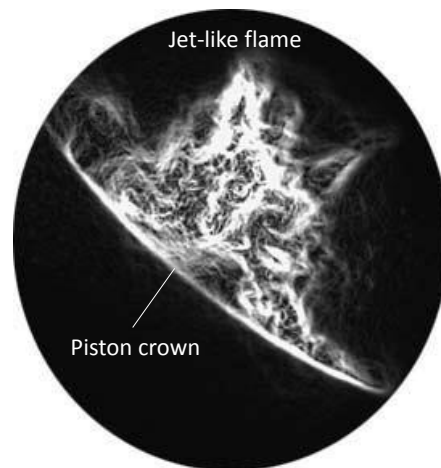


Figure 1. Picture taken at Chalmers laboratory of a jet-like flame impinging on the piston crown as a result of diesel injection in a heavy duty engine [19]

Impinging jets have been studied in a number of configurations varying in geometrical and dynamic parameters. The dynamic variables basically are related to the jet velocity and the level of turbulence in the flow [3, 5, 6, 9, 11]. A number of studies have been presented regarding stationary jets. On the other hand, in an ICE the jet has a cycling / pulsating nature but little is found in literature about this topic.

Impinging jets have been historically studied analytically and experimentally. Later, numerical simulations have also been deployed in this field. Numerical simulations are nowadays an established method to study and predict fluid flows. Therefore, they are widely used for product development in industry. Attempts to study impinging jets have been carried out using CFD (Computational Fluid Dynamics) simulations with varying degrees of success [7, 14, 15, 16, 18]. The general conclusion is that the more detailed the model the better it can capture the flow feature. However, detailed models are increasingly computationally expensive and have bigger stability problems. When considering industrial applications it is important to consider also the latter factors.

Reference [14], by the author of this work, addresses impinging jets with a steady state (time averaged) approach. In [14] it was concluded that transient phenomena can play an important role in the impingement process even if the flow is stationary. The present work extends the study with a transient analysis of stationary impinging jets. It compares the performance of different modelling parameters, including different turbulence models. The evaluation is not only based on the comparison with experimental data but also on the computational effort necessary to perform the simulation.

2 Impinging jet physics

2.1 Impinging jet flow features

A comprehensive description of impinging jets is presented in [10, 11]. Here a short description is given, in order to bring attention to some important features relevant to the present work. An impinging jet is characterized by a jet flow impacting (impinging) on a surface. The resulting flow field can be divided in 3 regions.

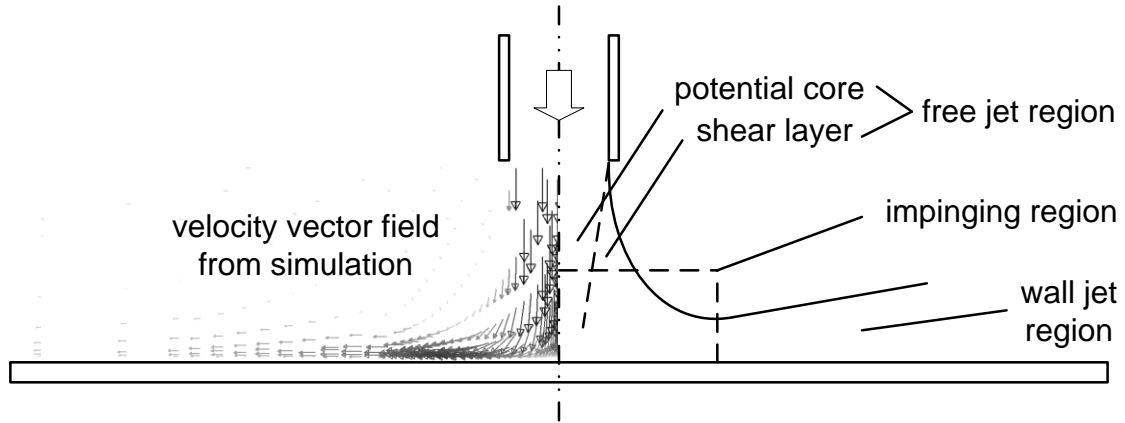


Figure 2. Impinging jet regions definition.

- The *free jet region* in which the wall is not affecting the flow field. This region can be further sub-divided in two. 1) The potential core where the flow basically maintains its initial velocity (nozzle outlet velocity). 2) The shear layer where the jet interacts with the surrounding medium exchanging momentum and mass.
- In the *impinging region* the flow strikes to the wall and is forced to undergo a sudden change of direction. The stagnation point is located at the center of this region.
- The *wall jet region* in which the flow leaving the impinging region develops into a semi-confined flow.

In the jet shear layer large parallel toroidal (donut-like) vortices interact with each other. Under certain flow conditions the vortices merge in an event called “vortex pairing” (see Figure 3), this is a case of turbulence back scattering. Back scattering is the transfer of turbulent kinetic energy from small to larger turbulent length scales. This is a known phenomenon typical of certain turbulent flows and it presents a difficulty for common turbulence models, which are designed assuming turbulence to be purely dissipative.

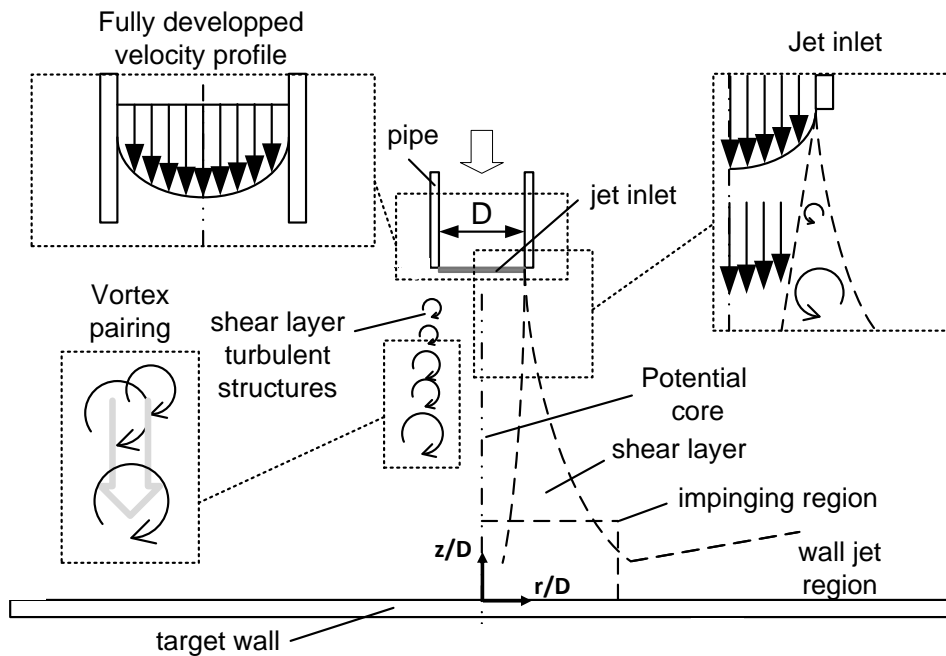


Figure 3. Physical processes in impinging jets.

Impinging jet flow has remarkable effects on convective heat transfer. Indeed, this kind of flow has among the highest known levels of Nusselt number (Nu) for single phase flows.

There are different types and configurations of impinging jets. A distinction can be made by the shape of the nozzle (circular, slot, or square). For example, a jet can be discharged from a pipe or from a hole giving different velocity profiles at the nozzle outlet, and the jet may be confined by an upper wall.

Unless otherwise stated, in this work *impinging jet* refers to the flow discharged from a circular pipe without confinement that is sufficiently long to ensure a fully developed turbulent flow. The jet is discharged in a quiescent (still) medium of the same nature as the jet flow. This is best described by Figure 3.

The nozzle diameter D is the reference length to characterize impinging jets. The most important parameters to describe impinging jets heat transfer are the two dimensionless groups Nusselt Number (Nu) and Reynolds number (Re). Geometrical parameters are the nozzle to wall spacing (z/D) and the radial position (r/D). Another important parameter is the inlet turbulence intensity. The final goal of the research on impinging jets is to understand the physics governing the phenomenon and correlate all these parameters.

2.2 Impinging jet heat transfer

Research on impinging jet in literature has been carried out experimentally, analytically and numerically. An example of experimental results is proposed in Figure 4. The Nusselt number presents a maximum in the stagnation point. Here the boundary layer thickness is at its minimum, offering the minimum resistance to the heat flux. The Nu then tends to decrease for greater r/D due to the growth of the boundary layer. Moreover, the radial flow velocity decreases as the flow spreads to an increasingly larger area.

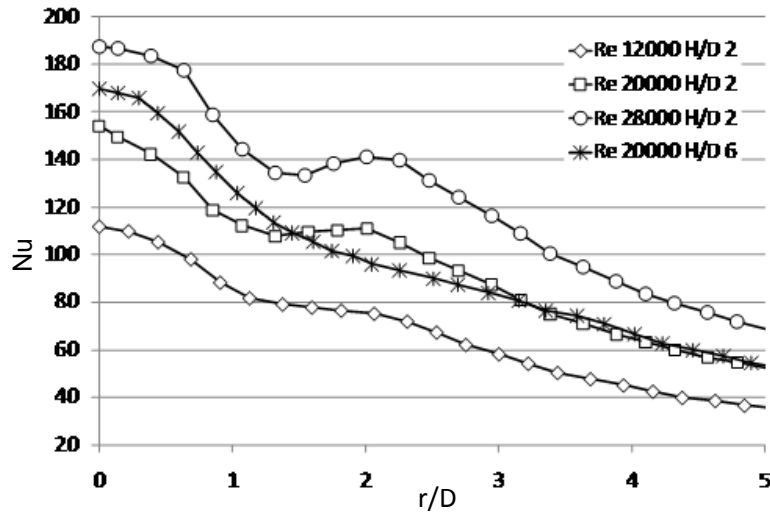


Figure 4. Experimental results $Nu(r/D)$ [2].

For relatively high Re and small z/D (e.g. $Re = 30000$ and $z/D = 2$) the Nusselt number variation in radial direction $Nu(r/D)$ presents a secondary peak (Figure 4). This phenomenon is not fully understood despite considerable experimental and numerical efforts [4, 5, 6, 8].

Various explanations are suggested to explain the characteristic secondary peak. One explanation is as follows: the free jet feeds the wall jet region as a column of fluid as shown in Figure 5. In the impingement region the flow diverges in radial direction forcing it to a strong angular acceleration creating the wall jet region. Strong acceleration holds the boundary layer laminar damping velocity fluctuations normal to the flow. Moreover, in the acceleration zone, the flow is pressed against the wall by the incoming column of fluid. The acceleration results in high velocity which in turn generates high heat transfer. As the radial distance increases, the velocity decreases because the cross-sectional area of the flow in the wall jet region increases.

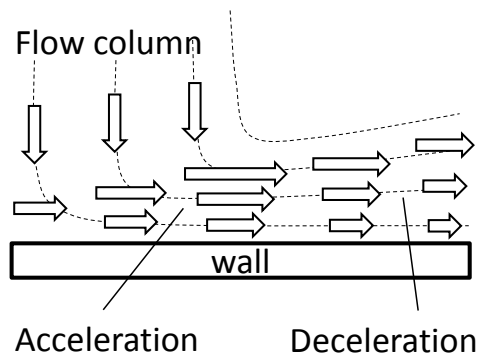


Figure 5. The acceleration-deceleration effect.

An alternative explanation relates to the development of the boundary layer. The laminar boundary layer develops from the stagnation point and eventually undergoes the transition to turbulent flow. The transition region is associated with an increase in heat transfer due to the enhancement of mass transfer in the direction normal to the wall. This transition is believed to be responsible for the secondary peak in the $Nu(r/D)$. The boundary layer development for an impinging jet is different from the one of a flat plate. An important cause of the difference is the radial flow velocity decreasing due to the radial increase of the cross-section area.

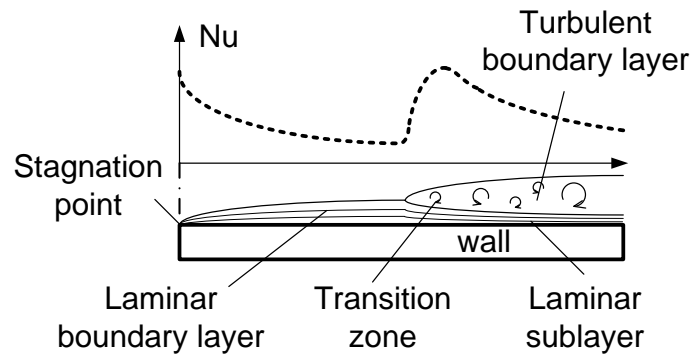


Figure 6. Effects of the development of the boundary layer on Nu (qualitative).

A third explanation for the secondary peak is that turbulent vortices grow in the shear layer of the free jet. These structures travel in the jet direction and impact on the target surface in a ring around the impingement point. The resulting velocity fluctuations normal to the wall increase the heat transfer affecting the boundary layer structure. This theory is supported by measurements [5, 6] correlating the vortices frequency with the fluctuation of the heat transfer rate.

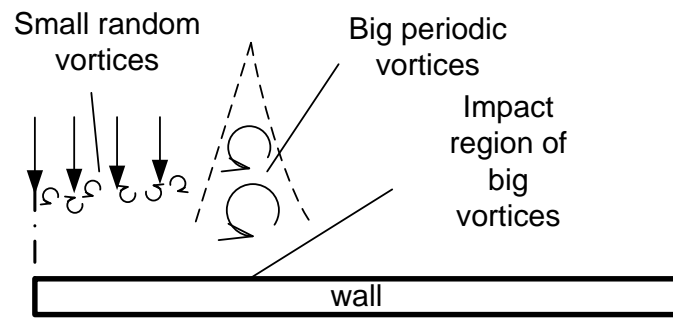


Figure 7. Shear layer vortex wall impact.

It is likely that the secondary peak in the Nusselt number curve is attributable to same combination of the three effects presented above. Interestingly, for very small values of z/D a third peak is observed, suggesting that the different phenomena act at different locations [10].

The heat transfer rate depends strongly on the jet inlet conditions such as the velocity profile. Different inlet conditions can result from different nozzles or from other factors. The inlet profile is affected by the shape of the piping upstream of the nozzle. Curvatures and cross section changes affect the velocity distribution. A repeatable configuration is obtained using a sufficiently long straight pipe of constant cross section so as to ensure that the flow at the nozzle has a fully developed velocity profile.

Another important parameter is the turbulence intensity. High levels of turbulence enhance the momentum diffusion of the jet and consequently reduce the potential core length. The effect of the turbulence is strong enough to eliminate the local minimum occurring for high Re and small z/D . However, this variable has a lower impact for higher z/D where the turbulence created in the shear layer becomes dominant [10, 11].

3 Modelling of impinging jets

3.1 Modelling methodology

A CFD model is a complex assembly of a number of interacting sub-models. For example, the way turbulence is handled and how the equations are numerically discretized. The choice of these sub-parts influences the final result. In this study a number of variables are tested and cross compared in order to serve as a future reference for setting up an efficient simulation for impinging “jet - like” flows. This section discusses each of the different parts of the model individually.

3.1.1 Time (temporal discretization)

The characteristics of a stationary jet can be meaningfully represented by a time-averaged solution. However, by resolving also the time variation of the flow it is possible to gain a deeper understanding of the phenomena governing the impinging jet. It is also known that some problems related to simulation stability can be overcome by running a transient simulation of a stationary problem. The downside of this approach is that it significantly increases the simulation’s computational cost. Another reason to approach the problem with a transient simulation is that the final application is to be in ICE combustion models in which case it is necessary to consider pulsating rather than stationary jets.

An important parameter in transient simulations is the CFL number, which is defined as

$$CFL = \frac{u\Delta t}{\Delta x}$$

Here, u is the generic velocity, Δt is the time step and Δx is the cell size in the u direction. Physically, this quantity defines how many cells a fluid particle passes through in a time step. For a robust transient simulation the CFL should be smaller than one. However, for practical reasons, a larger CFL number is often tolerated to speed up the calculation. For all simulations run in this project the time step is chosen so that the CFL number is around one for most of the domain, allowing temporary local maxima of about ten.

3.1.2 Space (spatial discretization)

The case in study is a jet issued by a long pipe and impinging orthogonally on a flat surface. Figure 8 provides an overview of the geometry along with details of the mesh and boundary conditions. The mesh defines how the geometry (or better the computational domain) is discretized in control volumes. The geometry is divided in 100 layers in direction normal to the impingement plane. The size of the cell layer closest to the impingement wall is chosen so that it satisfies the condition of $y^+ < 1$ in every locations. This condition is necessary to resolve the viscous sub-layer (see zoom-in in Figure 8). The circular shape of the domain is discretized using the “peacock” topology. This topology allows for a flexible increase in the number of cells in both the radial and the angular directions and gives better results than the more commonly used “o-grid” topology [15]. Three meshes are created with a total of 0,125, 0,5 and 2 million cells.

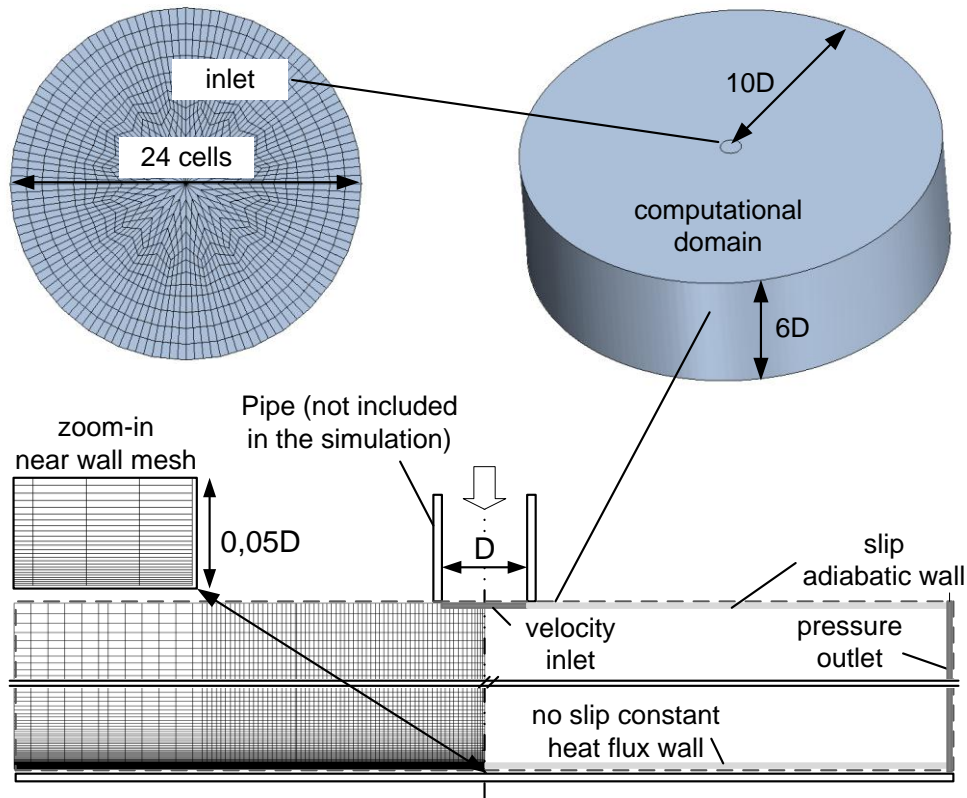


Figure 8. Computational domain, mesh and boundary conditions.

3.1.3 Wall and outlet boundary conditions

The computational domain extends sufficiently far in the radial direction to cover the impingement area with a good margin to prevent the boundary effects from influencing the area of interest. The outlet boundary condition is *pressure* (see Figure 8). The upper boundary condition is *slip wall*. This configuration defines a confined jet, while the experiments used for comparison refer to non-confined jets. A more realistic boundary condition for the upper wall would be *pressure*, which would allow the flow to cross the boundary but this condition is avoided because it is known to be more prone to numerical instability. This choice is backed by the measurements in [8] showing that the differences in heat transfer between confined and unconfined jets for $z/D \geq 2$ are negligible. The boundary condition on the impingement wall is *no slip wall* with a constant heat flux, which reproduces the behavior of the electrical resistor used in the experiments.

3.1.4 Inlet Boundary conditions

The inlet boundary condition is set as *velocity inlet*. The velocity profile for a fully developed pipe-flow is calculated in a separate simulation and mapped at the inlet boundary. The inlet boundary is discretized with 1280 cells in the inlet plane counting 24 cells in the radial direction (see Figure 8). This is fine enough to resolve the biggest

turbulent structure of the inlet flow. In the simulations run with this mesh, turbulent fluctuations are superimposed to the fully developed turbulent profile.

3.1.5 Inlet turbulent fluctuations

The turbulent fluctuations are calculated using the method presented in [12], only a brief overview is provided in this section. The method is specifically design to generate inlet boundary conditions to LES (Large Eddy Simulation) and DES (Detached Eddy Simulation). The turbulent integral length scale and time scale are derived from the inlet size and Reynolds number. A number of independent synthetized velocity fields are produced based on the turbulent integral length scale. The fields are independent in the sense that their time correlation is zero. When running the simulation, one of the computed velocity fields is superimposed as initial conditions for the inlet. The inlet condition for a given time step N is calculated as a weighted average between the fluctuation field N and the superimposed fluctuation field at $N-1$, this latter being function of all previously used fields. This interpolation is called an “asymmetric time filter” and is a function of the turbulent integral time scale and the simulation time step. From the above description it follows that to calculate the inlet conditions at a given time step it is necessary to retrieve the inlet conditions at the previous time step.

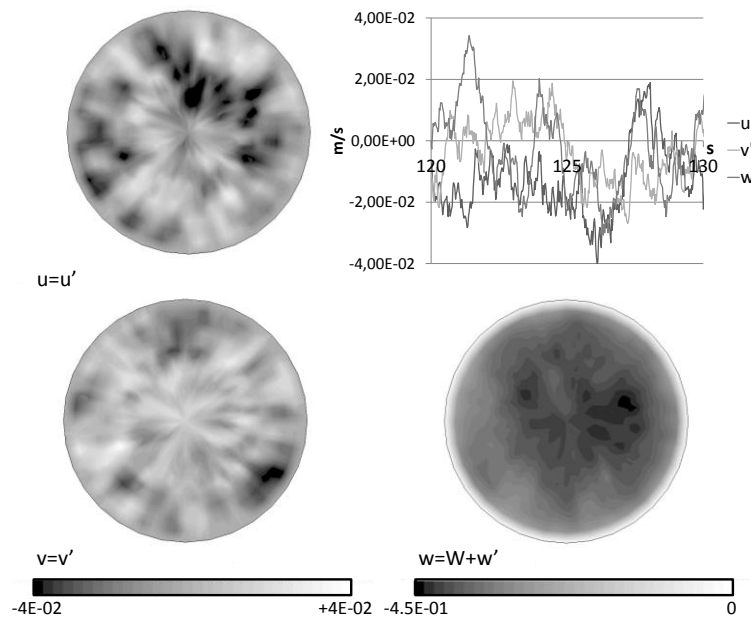


Figure 9. Example of synthetic fluctuations superimposed at the inlet. Instantaneous inlet flow field and time resolved fluctuations in one inlet boundary cell.

The result of the application of the method presented above is a space and time correlated field of the velocity fluctuations at the inlet. Figure 9 shows an example of these fluctuations. The graph shows the variation in time for the three components of the velocity fluctuation (u' , v' and w') for one of the inlet cell. It can be noticed as the three fluctuation components are of the same order of magnitude. Consequently, at the inlet the cell aspect ratio should be about one to properly resolve the fluctuations. In the sub-figure

presenting the jet axial velocity (w), it is also possible to appreciate the profile of the average inlet velocity (W). This grows in magnitude from zero at the boundary to its maximum in the center. On top of this profile are superimposed the w' fluctuations.

3.1.6 Equations (numerical discretization)

The simulations are carried out using STAR-CD. This commercial code can be run with its own patented discretization scheme called MARS. This is a second order discretization scheme. The MARS ability to capture strong gradients in the flow can be changed by using different setting for the scheme's compression level. This can be changed between 0 and 1. Low values for this parameter result in a more robust model, less prone to diverge or crash. With higher values of this parameter the simulation is more likely to capture more accurately sharp gradients in the flow field. The default value for this parameter is 0,5 which is a compromise between accuracy and convergence rate." The same differentiation scheme is used for all the equations (i.e. momentum, energy and turbulence). The Central Difference (CD) scheme is also tested in one case for comparison.

3.2 Turbulence modelling

With the current computational resources it is not possible to resolve all the turbulent structures. Consequently, we are left trying to model turbulence. The different approaches to turbulence modelling are based on assumptions that allow simplification of the problem. The quality of the results depends then on how well these assumptions fit the problem under study. In this respect impinging jets are a recommended test for the evaluation of turbulence models. Indeed, they present peculiar turbulent structures that are not well represented by the common assumptions on which many turbulence models are developed, as discussed in [16].

Most models exist in two forms, high-Re and low-Re. The low-Re form implies that no wall function is implemented in the model and the boundary layer is resolved down to the viscous sub-layer. This approach is recommended for cases in which the boundary layer is not fully developed (e.g. impinging jets). For this reason all models used in this study are in their low-Re form, for the same reason the mesh is generated so as to resolve the boundary layer accurately enough as described in 3.1.2.

In this work four different turbulence models are tested: a brief description is given below, and further details are gathered in the Appendix: Turbulence models description. All simulations are run with the commercial code Star-CD licensed by CD-Adapco. The specifics of the model are the ones implemented in version 4.08 of the code.

3.2.1 k- ϵ model (standard)

A basic assumption is that the dissipative effect of turbulence can be accounted for with a scalar isotropic property called turbulent viscosity μ_t (Bousinesq approximation). Turbulent viscosity is calculated locally in the computational domain and is related to the local turbulent length and velocity scales. The production terms in the transport equation of turbulent quantities are related to the local gradients of the mean flow.

The k- ϵ model is a result of the implementation of the assumption above. In this model all turbulent quantities are derived from the turbulent kinetic energy k and the turbulent dissipation rate ϵ . The turbulent viscosity μ_t is computed from k and ϵ . The transport equations for these two quantities are resolved along with the momentum and energy equations.

The k- ϵ model belongs to the family of the two-equations models. These models are called so because they solve turbulence with two equations. A rather extensive study of two-equations models applied to impinging jets is presented in [16]. The general conclusion of the study is that this type of models is not particularly suitable to solve impinging jet flows. In the same work, the specific results for impinging jets with characteristics similar to the present study indicate that the standard k- ϵ model performs best. Moreover, the k- ϵ model is the most popular of the turbulence models used in industry. For these reasons it is considered in this investigation, although expectations are scarce regarding the results. In fact, the assumption above do not properly represent impinging jet flows, since the turbulent characteristics of impinging jets are not isotropic. This is clear in at least two locations:

- In the shear layer the turbulent structures are oriented such as to form toroidal structures around the jet.
- Close to the wall, and in particular in the impingement zone, turbulent fluctuations are affected by the presence of the wall.

A complete description of the k- ϵ model can be found in [13].

3.2.2 V2F model

The pressure strain affects the turbulent structures in the near wall region of an impinging jet. The V2F model differs from the k- ϵ model in that it solves for two extra quantities, the wall normal Reynolds stress v^2 , and f_{22} , which is an equation for the redistribution of v^2 . The physical interpretation of v^2 is the Reynolds stress normal to the closest wall, with the coordinate system used in this work this is $\overline{w'^2}$. The V2F model automatically detects the presence of a wall and accounts for its effect on the turbulence.

3.2.3 LES (Large Eddy Simulation)

In a turbulent flow it is possible to make a distinction between the turbulent structures, or eddies, according to their size. The largest eddies are often well recognizable structures in the mean flow, these structures extract kinetic energy from the mean flow field. The largest eddies size is in the order of the geometry and their time scale in the order of the mean flow hence to assume them as isotropic is a coarse simplification. The energy collected in the large eddies is passed down to smaller and smaller eddies. In this cascade it becomes more and more difficult to distinguish the turbulent structures and the isotropic assumption becomes more representative. In the smallest eddies the energy is dissipated by viscous effects and goes to increment the flow internal energy (heat).

The basic idea behind LES models is to resolve the largest turbulent scales. Consequently, it is necessary to run a three-dimensional, time-dependent computation with a mesh fine enough to resolve the large eddies. Figure 9 is a good example of the

large eddies resolution. The effects of eddies with smaller length scales are accounted for with a sub-grid model. The different LES models differ in how the small eddies are modelled. In this work we use the Smagorinsky model because it is the simplest and most commonly used.

3.2.4 DES (Detached Eddy Simulation)

In the near wall regions the largest turbulent structures are relatively small. Their size is indeed in the order of the turbulent boundary layer thickness. The boundary layer effects are very important and they need to be accurately accounted for. This leads to a very high computational effort when using LES models. These difficulties lead to the use of a hybrid method called DES. In this type of models the main flow is resolved with the LES approach while the near wall region is modelled with a RANS models. The RANS model chosen in this study is the standard k - ϵ described in section 3.2.1.

The switch between LES and RANS models is handled locally comparing the cell size with the eddy length scale.

4 Transient modelling results and discussion

4.1 Experimental reference

The transient simulations are run at $Re = 23000$ and $r/D = 6$. Three sets of experimental results achieved with similar measurement methods are found in literature (see Figure 10).

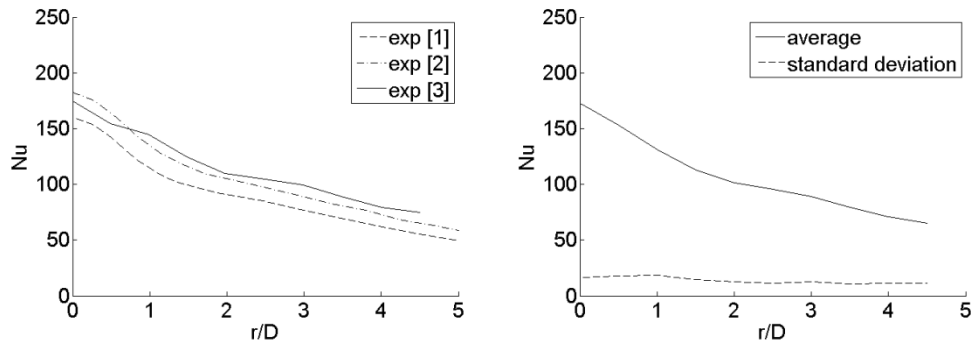


Figure 10. Experiments at $z/D = 6$. Baughn_1989 [1] at $Re = 23750$. Katty 2008 [2], Lytle 1994 [3] at $Re = 23000$.

Another author [5] presents data for the Nu at different Re. The measurements shows similar curves to the ones presented in Figure 10 but are sensibly lower in magnitude. This difference is probably due to the different measurement technique. Interestingly, [5] reports also data for the root mean square (rms) of the Nusselt number, which is measured to be approximately 10% of the Nu at the stagnation point.

4.2 Simulation results

The averaging for post-processing is done on 100s simulated time. Previous to post processing, the simulations are run for 100s: in this time the jet flushes the computational domain in z direction (i.e. inlet to wall) about 6 times. The results are presented as the average calculated for constant radii.

The main focus is on the heat transfer coefficient (i.e. the Nusselt number). Some quantities describing the turbulence in the jet flow are also reported. These are normalized with the jet bulk velocity at the nozzle outlet W_b .

The results are cross-compared to study the effect of the different parameters and the available experiments.

4.3 Results from LES simulations

4.3.1 Mesh size effects

Two different mesh topologies are tested with the same number of cells, Figure 11 shows them. Both meshes are identical for $z/D < 0.5$. Mesh 1 has a constant cell size in the jet direction for $0.5 < z/D < 6$. Mesh 2 grows geometrically from the impingement wall to the upper boundary, resulting in cells with an aspect ratio of about 5 at the inlet. Mesh 1 is used in all other simulations. Comparing the results from mesh 1 and mesh 2 it can be noted that a finer mesh at the inlet is necessary to capture the turbulence fluctuations which are otherwise dampened due to the larger cell size.

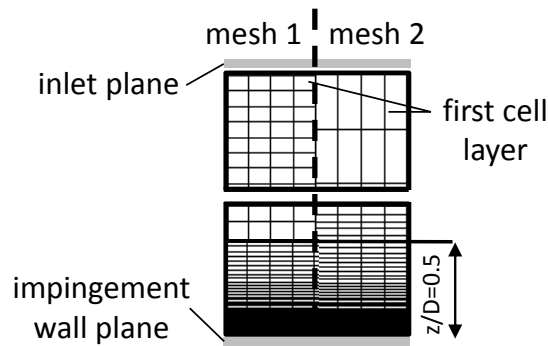


Figure 11. Zoom-in of mesh resolution close to the inlet and to the wall for the two different meshes.

Figure 12 a) shows the effect of cell size on the turbulent fluctuations near the inlet. With mesh 2 the cells are too big to resolve these fluctuations and they are dampened, consequently the level of turbulence is under predicted. The same picture shows how the fluctuations are better resolved with mesh 1. The resolved turbulence kinetic energy k is of the same order of the one expected in a fully developed pipe flow (“ k pipe” in the figure).

Figure 12 b) shows the modelled turbulent kinetic energy k computed for the sub grid model (described in Appendix: Turbulence models description). In the region at $r/D = 0,5$ there is a strong velocity gradient between the jet exiting from the nozzle and the quiescent fluid. This works in the k equation resulting on a peak in the modelled k .

At $z/D = 0,5$ the cell size is alike for the two cases. Figure 12 c) shows that the resolved k has similar values for both meshes in particular for $r > D/2$. In this figure it is visible that the effect of the shear layer results in levels of k that are almost one order of magnitude higher than at the inlet.

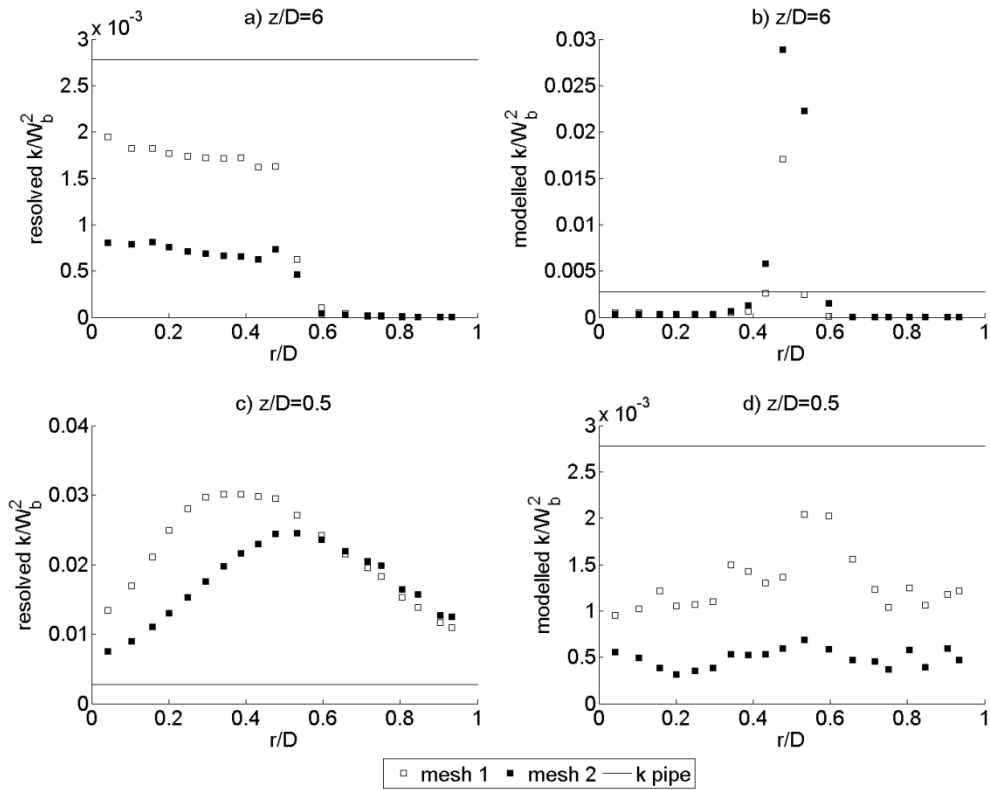


Figure 12. Effects of mesh topology on resolved and modelled k . For comparison “ k pipe” is included which is the turbulence kinetic energy expected in a fully developed flow in a straight pipe at the same Re .

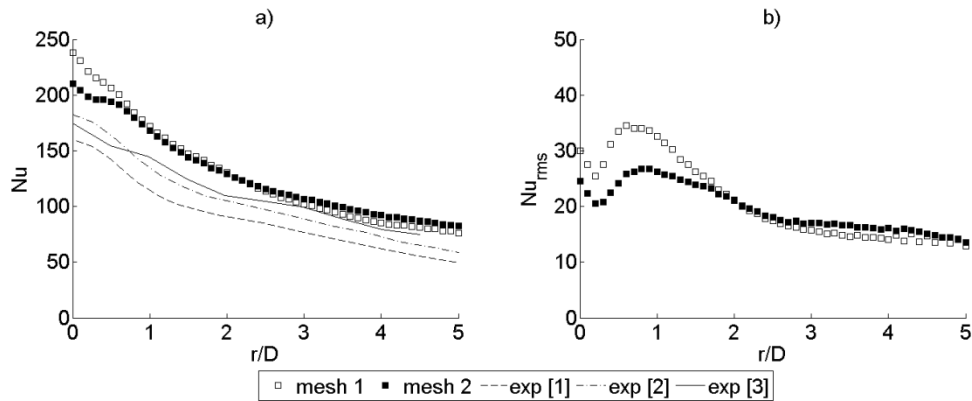


Figure 13. Effect of mesh topology on Nu and Nu_{rms} .

Figure 13 shows that the mesh has a relatively small effect on the predicted Nu and Nu_{rms} . Indeed close to the wall the two meshes are identical and the incoming turbulent flow field is very similar as shown in Figure 12 c). This, understandably, leads to similar results at the wall surface.

4.3.2 Effects of the numerical discretization

The simulations are carried out using STAR-CD. This commercial code can be run with the MARS discretization scheme presented in 3.1.6.

The same differentiation scheme is used for all transport equations. Three cases are run with a different value for the MARS parameter: 0, 0,25 and 0,5. As mentioned in section 3.1.6, a low value for the parameter gives a more robust but less accurate solution and vice versa. Figure 14 a) and b) show no relevant differences varying the MARS parameter between cases. This is because at the first cell layer the differentiating scheme has no “time” to affect the solution. Further downstream (see Figure 14 c) and d)) a low value for the MARS parameter dampens the resolved turbulence fluctuations. The same effect can be seen also on the Nusselt number fluctuations (Nu_{rms}) in Figure 15 b). On the other hand no sensible difference is appreciable on the average Nu (Figure 15 a)).

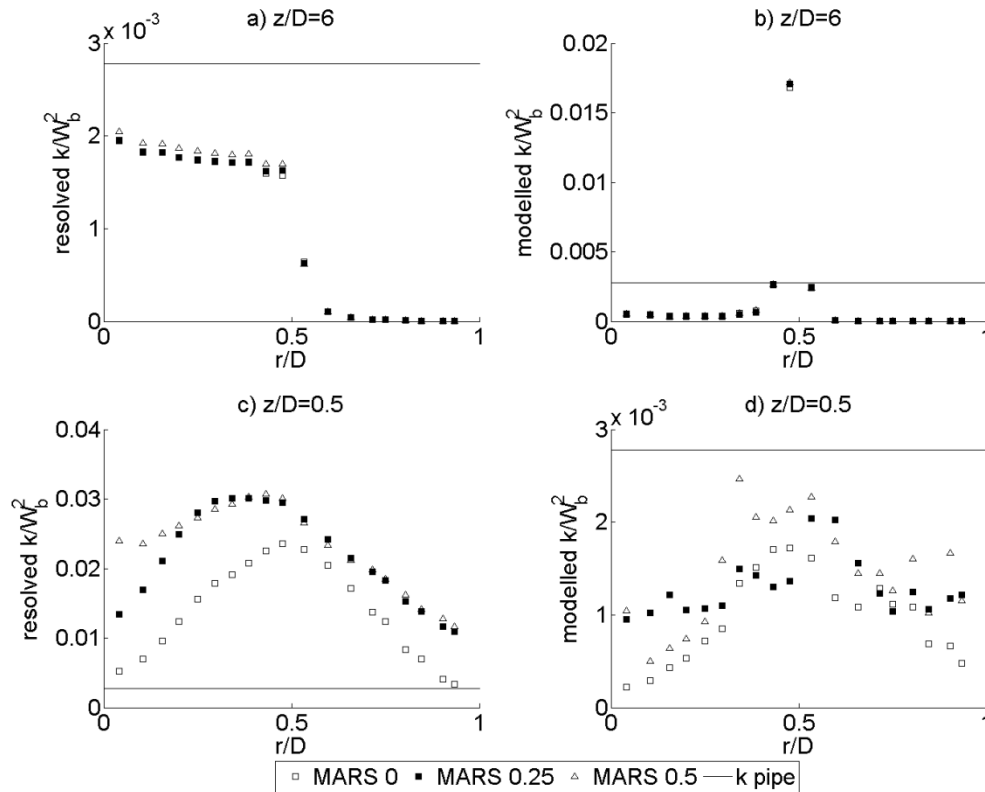


Figure 14. Effects of differentiating scheme on resolved and modelled k .

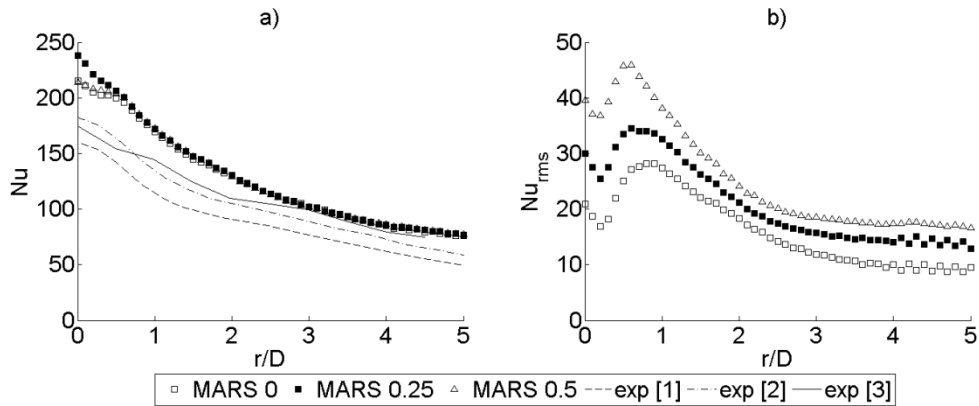


Figure 15. Effect of differentiating scheme on Nu and Nu_{rms}.

In the literature, use of the CD scheme is recommended for LES simulations at least for the momentum equations. A few attempts to apply this scheme gave no good results in terms of heat transfer (see Figure 16). For turbulent quantities as shown in Figure 17 the CD scheme gives somehow better results. This scheme has a lower (or null) dampening effect on the fluctuations and results in local peaks. In the region close to the wall the resolved turbulent kinetic energy (Figure 17 c)) is very similar for both schemes. This region is dominated by the turbulence created in the shear layer.

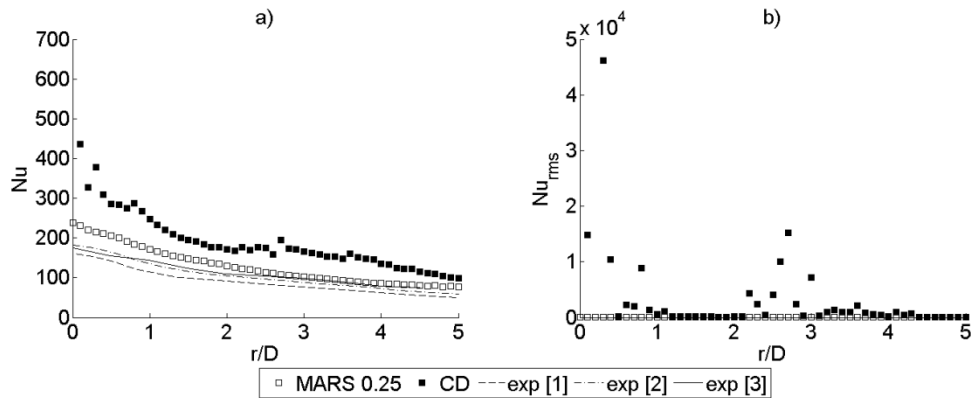


Figure 16. Effect of differentiating scheme on Nu and Nu_{rms}.

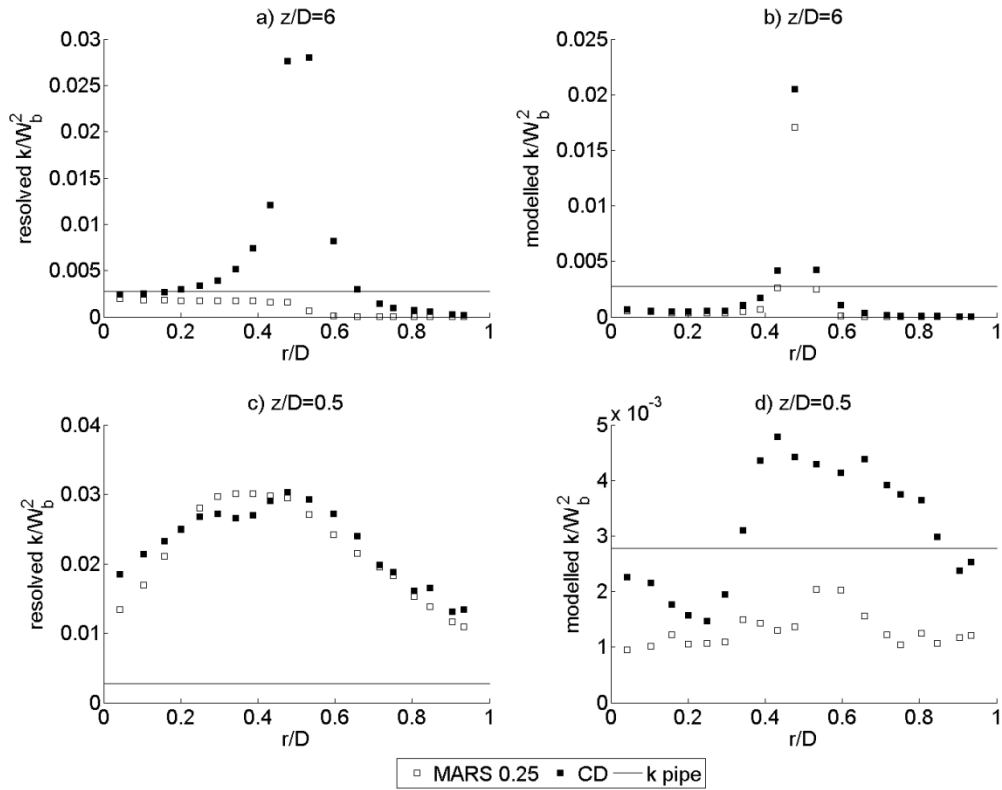


Figure 17. Effects of differentiating scheme on resolved and modelled k.

4.3.3 Effect of run time

All simulations are run for 200s simulated time and the averaging is done on the last 100s. To check the statistical relevance of this average, a case is run for a longer period, computing averaging over 300s. Figure 18 shows no difference between the two different runs validating 100s as a sufficiently long time for averaging.

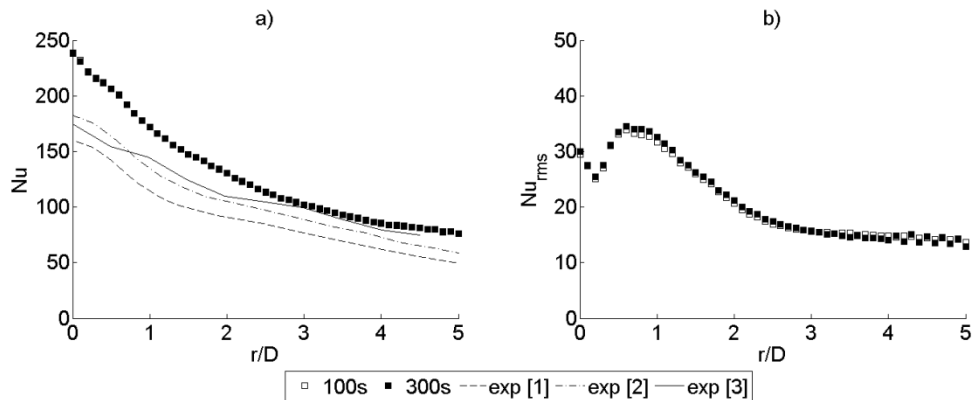


Figure 18. Effect of averaging time on Nu and Nu_{rms} .

4.3.4 Effect of inlet turbulence

The effect of inlet turbulence is studied by halving and doubling the inlet velocity fluctuations with respect to a reference run. This results respectively in a decrease to 25% and an increase to 400% of the resolved turbulent kinetic energy k . Figure 19 a) shows the effect of the inlet boundary condition close to the inlet. Further downstream (Figure 19 c)) the fluctuations are of similar magnitude in all cases. The level of turbulence here is much higher than at the inlet and depends mainly on the turbulence generate in the shear layer. The results for the Nusselt number presented in Figure 20 a) shows that the inlet turbulence level does not affect the average Nu outside the impingement region. In the impingement region ($r/D < 0,5$) the results differ for some 15% between each other. However, these do not follow a proportional correlation between increasing inlet turbulence and increasing Nu. A correlation can be notice between the Nu (Figure 20 a)) and the modelled turbulent kinetic energy in the proximity of the wall (Figure 19 c)) suggesting that this parameter is more important than others.

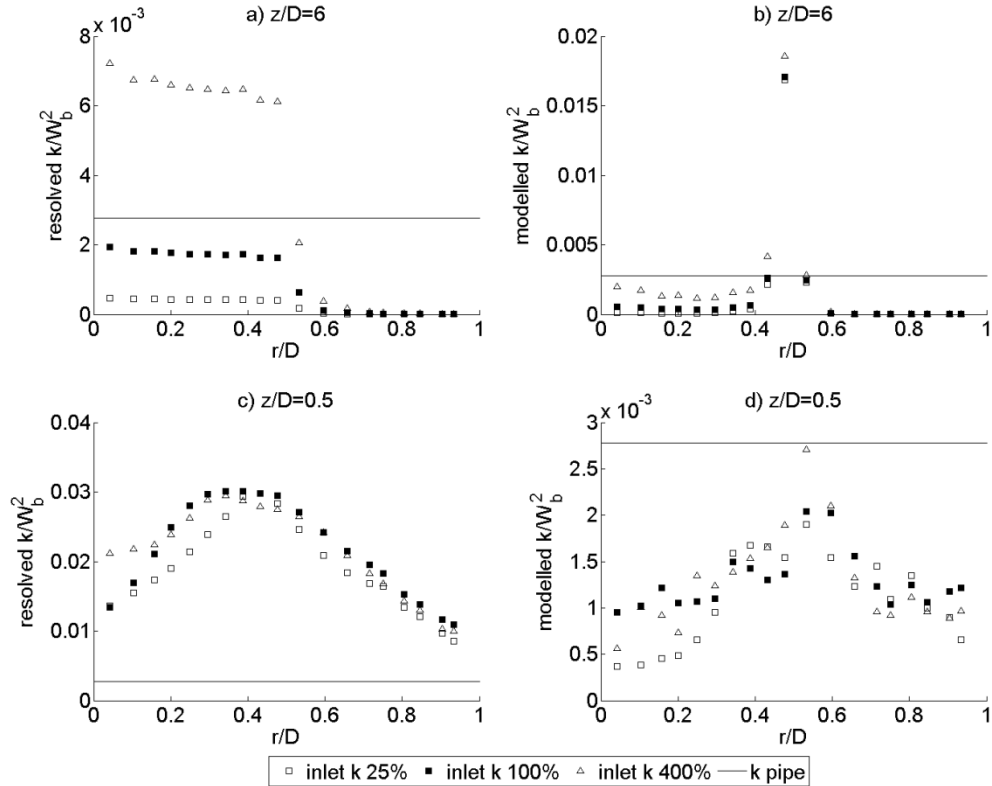


Figure 19. Effects of inlet turbulence on resolved and modelled k .

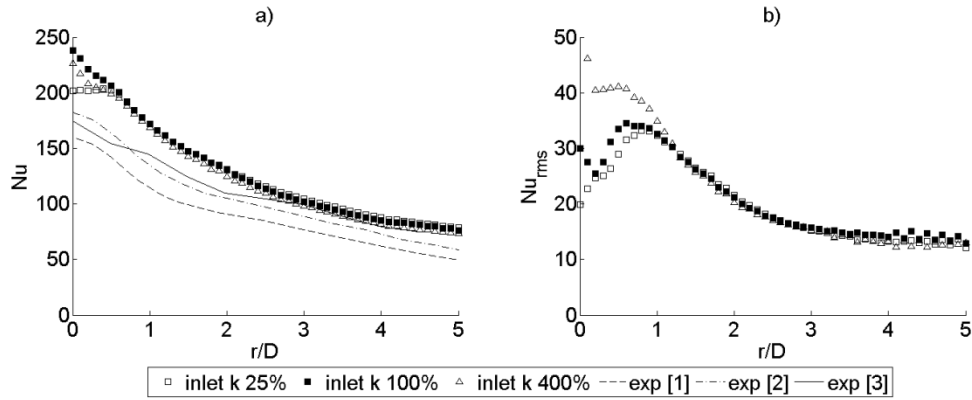


Figure 20. Effect of inlet turbulence on Nu and Nu_{rms} .

4.3.5 Resolved k vs. measurements

This section compares the results of flow field variables with the measurements presented by [16]. Only the results from simulations with LES turbulence model are considered. In general, the simulations capture the magnitude of both the velocity magnitude and the radial velocity fluctuations u'_{rms} . The largest discrepancies are noticeable close to the wall. The discretization order has a strong influence on the results, Figure 21 b) shows that the simulations run with growing values for the MARS scheme parameter result in larger fluctuations near the wall. These results are in agreement with the ones of Figure 15 b).

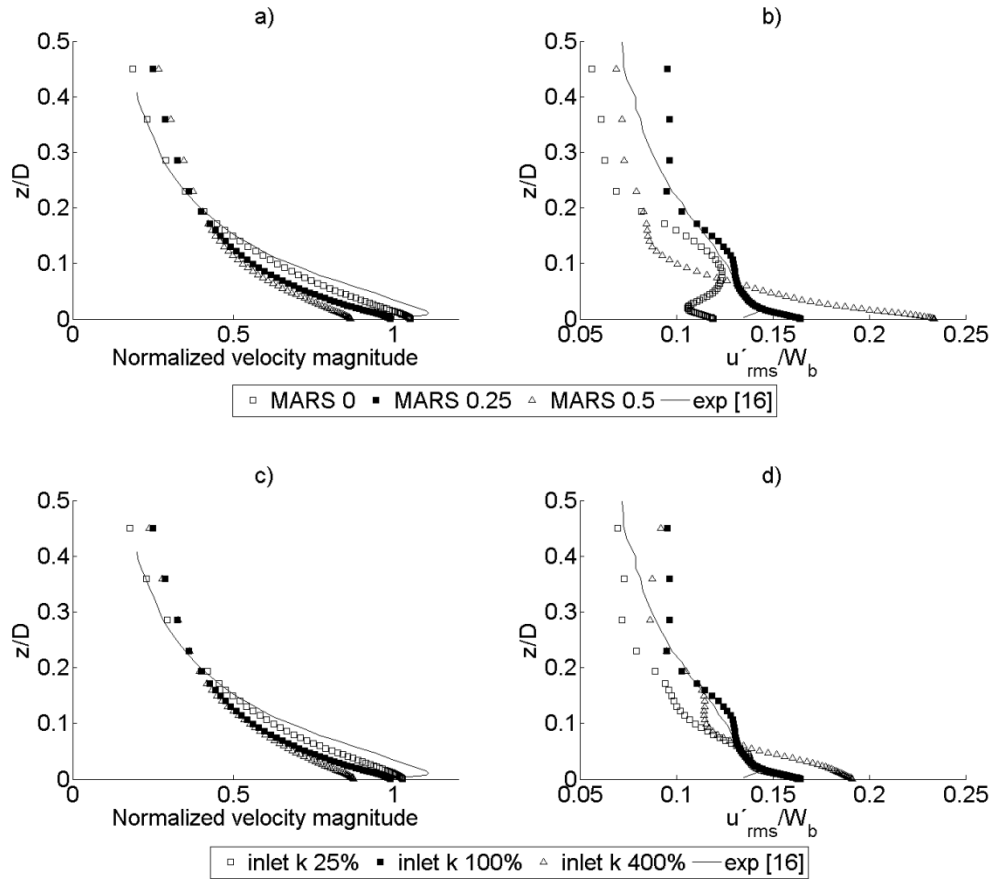


Figure 21. Velocity magnitude and radial velocity fluctuation (u_{rms}) at $r/D = 1$.

4.4 Heat transfer, comparison between LES, DES, $k-\epsilon$ and V2F

Simulations are performed to cross compare the different turbulence models presented in chapter 0. The different models are compared based on their prediction of the heat transfer between the jet and the wall, since this is the main focus of this study.

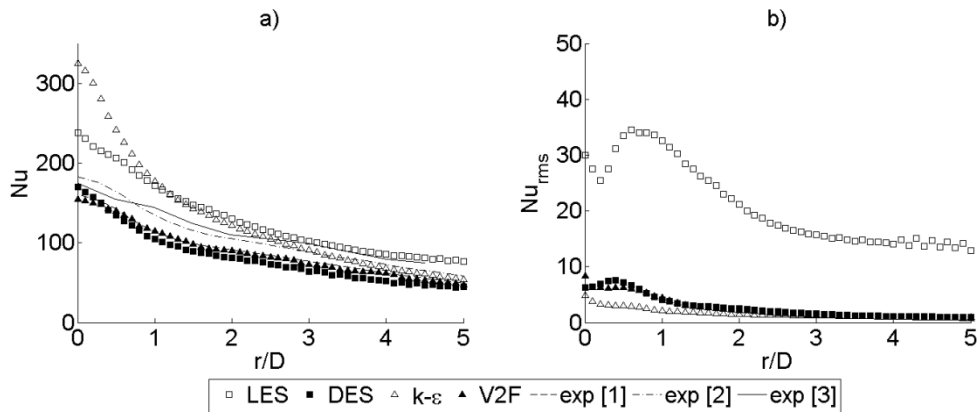


Figure 22. Effect of turbulence model on the Nu.

Figure 22 a) shows the average Nusselt number predicted by different turbulence models. As expected, the $k-\epsilon$ model over-predicts the Nu at the stagnations point getting closer to the measured one only for higher r/D . The V2F model slightly under predicts the Nu over the entire range of r/D . The DES model show results very similar to the V2F in almost the entire range of r/D . The LES model over predicts the experimental results in the entire range of r/D 's and this is the case for all the tests done with this model as presented in the previous sections.

The LES model predicts the Nu_{rms} to be 10-15% of the average Nu at the stagnation (see Figure 22 b)). This correlates well with the data presented in [5]. The other turbulence models under predict the Nusselt number fluctuations. This behavior is expected from the $k-\epsilon$ and V2F models in which turbulent fluctuations are very much dampened. On the other hand, a similar behavior is shown even for the DES model, even though this model should resolve the fluctuations similarly to the LES model.

The results regarding the Nu_{rms} can be further explained considering how turbulence is resolved by the different models upstream the impingement wall (Figure 23). The LES model resolves the major part of the turbulent velocity fluctuations. All other models do not capture the fluctuations, the turbulence is modelled instead. The DES model shows characteristics very similar to the $k-\epsilon$ and V2F model indicating that it is working in RANS mode. At $r/D = 0$ the modelled k is very similar between the DES and the $k-\epsilon$ model but this does not find match with the result about the Nu presented in Figure 22 a).

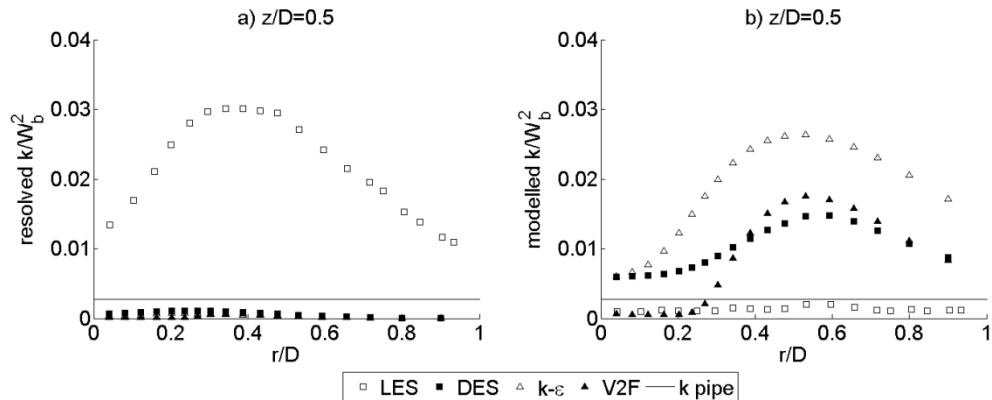


Figure 23. Resolve and modelled turbulence in the vicinity of the impingent wall, comparison of different turbulence models.

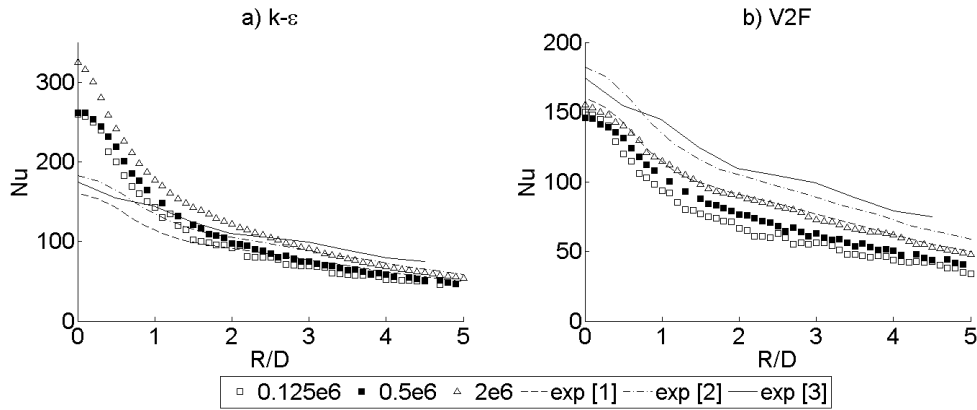


Figure 24. Effect of mesh density on the Nu.

The effect of the mesh density for the k-ε and V2F model can be seen in Figure 24. Three different meshes are tested with 0.125e6, 0.5e6 and 2e6 cells. The k-ε model does not perform well particularly in the impinging region. It can be also noted that this model performs the worst with the higher mesh density. A possible source of the difference between these results is that only the simulations with 2e6 cells are carried out applying the synthetic fluctuations at the inlet. However, considering Figure 19, this should not have a significant influence. The V2F model slightly under predicts the level of Nusselt number in the entire range, giving quite satisfactory results, particularly with the finest mesh.

4.5 Computational cost

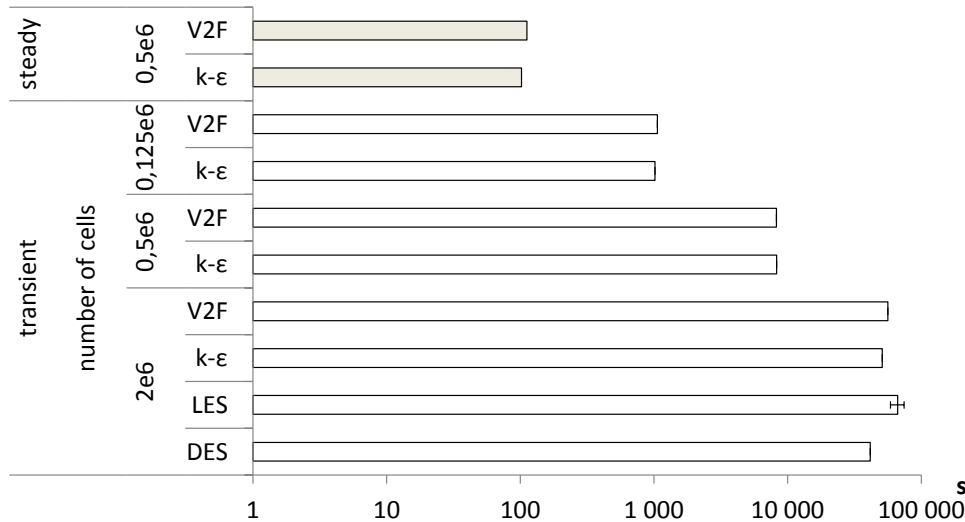


Figure 25. CPU time per simulated second. More than one simulation is run with the LES model, the error bar is the standard deviation.

Figure 25 presents the time necessary for one CPU to compute one second of simulated time. This time is affected by many factors such as the number and type of CPUs used. Another important factor is the need to solve extra subroutines. These are for example the two extra subroutines used for the implementation and post processing of the synthetic

fluctuation. In parallel computing, communication between CPUs is a significantly time-consuming process. The domain is partitioned in clusters of cells and each cluster is assigned to a CPU. At the end of each iteration, the solution at the cluster boundaries needs to be passed to the CPU(s) computing for the adjacent cell(s).

For the reasons presented above, the data from Figure 25 can be treated only as something indicative, since different types of CPUs were used, as well as different partitions. It can be noticed that the V2F is slightly slower than the k- ϵ model. This is probably due to the fact that the V2F model solves for two extra equations. Six simulations with the LES model are run with the same CPU configuration. The standard deviation for the runtime of these simulations is about 11%, as shown in the error bar in Figure 25. The DES model is relatively fast compared with the other ones tested; further study is however necessary to better assess this model since in this study only one simulation is run with it. In Figure 25 the computational cost related to the growing number of cells can also be appreciated. The same figure also shows the computation time for steady state simulations for comparison.

5 Conclusions

The objective of this work is to evaluate different approaches to the simulations of impinging jets. The test and cross-evaluation of several different models is useful when deciding how to address this kind of flow.

Considering turbulence models, the k - ϵ model is verified to be not sufficiently accurate in predicting heat transfer. The V2F model is slightly more computationally expensive but gives significantly better results, even with a relatively coarse mesh. The V2F model slightly under predicts the heat transfer compared to the experimental results. The DES model gives results very similar to the V2F model and should be considered for simulations of this kind, although it must be mentioned that this model is studied only briefly in this work. Furthermore, the results from the heat transfer fluctuations indicate that the k - ϵ , the V2F and the DES models do not capture the transient dynamic of the flow. In other words, they act much like their respective steady state simulation.

The LES model is studied more extensively, changing a number of parameters. This model is capable of resolving the turbulent structures in the shear layer in a satisfactory manner. The results are good both in terms of heat transfer prediction and flow-field turbulent characteristics. Only relatively little differences are noted when changing the various parameters. The only exception is the CD equation discretization scheme, the use of which gives adversely affected the predicted heat transfer. In general, the LES turbulence model over predicts heat transfer, compared with the experimental measurements. Unfortunately, this method is inherently expensive, since it requires both a fine mesh and a transient simulation, exponentially increasing the computational cost.

Using the LES model it is possible to verify that inlet turbulent fluctuations play only a minor role in the heat transfer phenomenon compared to the turbulence produced in the shear layer. This is true at least for the nozzle-to wall distance z/D studied in this work.

Nowadays, numerical simulations are used to study the combustion chambers of internal combustion engines. To date, most such simulations have focused on the combustion process. However, for many reasons, there is a growing need to consider the thermal interaction with combustion chamber walls. The results presented in this work will be used as a reference in order to improve the ability of ICE simulations to accurately account for heat transfer effects.

References

1. Baughn, J. W. and Shimizu, S. [1989], Heat transfer measurements from a surface with uniform heat flux and an impinging jet, *ASME J. Heat Transfer* 111/1097.
2. Katti, V. and Prabhu, S.V. [2008], Experimental study and theoretical analysis of local heat transfer distribution between smooth flat surface and impinging air jet from a circular straight pipe nozzle, *Int. J. Heat Mass Transfer* article in press.
3. Lytle, D. and Webb, B.W. [1994], Air jet impingement heat transfer at low nozzle plate spacings, *Int. J. Heat Mass Transfer* 37 1687–1697.
4. Gao, N., Sun H. and D. Ewing [2003], Heat transfer to impinging round jets with triangular tabs, *Int. J. Heat Mass Transfer* 46 2557–2569.
5. O'Donovan T. S. and Murray D. B. [2007], Jet impingement heat transfer – Part I: Mean and root-mean-square heat transfer and velocity distributions, *Int. J. Heat and Mass Transfer* 50 3291–3301.
6. O'Donovan T. S. and Murray D. B. [2007], Jet impingement heat transfer – Part II: A temporal investigation of heat transfer and local fluid velocities, *Int. J. Heat and Mass Transfer* 50 3302–3314.
7. Yue-Tzu Yang, Shiang-Yi Tsai [2007], Numerical study of transient conjugate heat transfer of a turbulent impinging jet. *Heat and Mass Transfer* 50 799–807.
8. Gao N. and Ewing D. [2006], Investigation of the effect of confinement on the heat transfer to round impinging jets exiting a long pipe, *Int. J. of Heat and Fluid Flow* 27 33–41
9. Koseoglu M.F. and Baskaya S. [2007], The effect of flow field and turbulence on heat transfer characteristics of confined circular and elliptic impinging jets, *Int. J. of Thermal Sciences* article in press.
10. Viskanta R. [1993], Heat transfer to impinging isothermal gas and flame jets. *Experimental Thermal and Fluid Science* 6:111-134
11. K. Jambunathan, E. Lai, M. A. Moss and B. L. Button [1992], A review of heat transfer data for single circular jet impingement, *Int. J. Heat and Fluid Flow*, Vol. 13, No. 2 106-115
12. L. Davidson [2007], Using isotropic synthetic fluctuations as inlet boundary conditions for unsteady simulations. *Advances and applications in Fluid Mechanics*, Vol. 1 Issue 1 1 - 35
13. Lien, F.S., Chen, W.L. and Leschziner, M.A. [1996], Low-Reynolds-Number Eddy-Viscosity Modelling Based on Non-linear Stress-Strain/Vorticity Relations, *Proc. 3rd Symp. on Engineering Turbulence Modelling and Measurements*, Crete, Greece.
14. M. Angioletti a, E. Nino a, G. Ruoccob, CFD turbulent modelling of jet impingement and its validation by particle image velocimetry and mass transfer measurements, *International Journal of Thermal Sciences* 44 (2005) 349–356
15. M. Bovo et al, On the numerical modelling of impinging jet heat transfer, *Int. Symp. on Convective Heat and Mass Transfer in Sustainable Energy*, 2009, Tunisia

16. Cooper, D., Jackson, D. C., Launder, B. E. & Liao, G. X. 1993 Impinging jet studies for turbulence model assessment-I. Flow-field experiments. *Int. J. Heat Mass Transf.* 36, 2675–2684.
17. H. M. Hofmann, R. Kaiser, M. Kind, H. martin, Calculations of steady and pulsating impinging jets—an assessment of 13 widely used turbulence models, *Numerical heat transfer, part b*, 51: 565–583, 2007.
18. Thomas Hällqvist 2006, Large Eddy Simulation of Impinging Jets with Heat Transfer KTH Mechanics, SE-100 44 Stockholm, Sweden, dissertation thesis.
19. Tobias Husberg, Savo Gjiria and Ingemar Denbratt, Piston Temperature Measurements by use of thermographic phosphors and thermocouples in a heavy-duty diesel engine run under partially premixed conditions, SAE 2005-01-1646

6 Appendix: Turbulence models description

This appendix reports the specific equations implemented in Star-CD for the different turbulence models.

6.1 Standard k- ε

The equation for the turbulent kinetic energy, k, is as follows

$$\frac{\partial}{\partial t}(\rho k) + \frac{\partial}{\partial x_j} \left[\rho \bar{u}_j k - \left(\mu + \frac{\mu_t}{\sigma_k} \right) \frac{\partial k}{\partial x_j} \right] = \mu_t \left(2S_{ij} \frac{\partial \bar{u}_i}{\partial x_j} \right) - \rho \varepsilon$$

with

$$S_{ij} = \frac{1}{2} \left(\frac{\partial \bar{u}_i}{\partial x_j} + \frac{\partial \bar{u}_j}{\partial x_i} \right)$$

$$\mu_t = f_\mu \frac{C_\mu \rho k^2}{\varepsilon}$$

$$f_\mu = [1 - e^{-0.0198 Re_y}] \left(1 + \frac{5.29}{Re_y} \right)$$

$$Re_y = \frac{y \sqrt{k}}{\nu}$$

The equations for the turbulent dissipation rate ε for the k- ε model is the following

$$\begin{aligned} \frac{\partial}{\partial t}(\rho \varepsilon) + \frac{\partial}{\partial x_j} \left[\rho u_j \varepsilon - \left(\mu + \frac{\mu_t}{\sigma_\varepsilon} \right) \frac{\partial \varepsilon}{\partial x_j} \right] \\ = C_{\varepsilon 1} \frac{\varepsilon}{k} \left[\mu_t \left(2S_{ij} \frac{\partial u_i}{\partial x_j} + P' \right) \right] + C_{\varepsilon 2} (1 - 0.3e^{-R_t^2}) \rho \frac{\varepsilon^2}{k} + C_{\varepsilon 4} \rho \varepsilon \frac{\partial u_i}{\partial x_i} \end{aligned}$$

with

$$P' = 1.33 [1 - 0.3e^{-R_t^2}] \left[2S_{ij} \frac{\partial u_i}{\partial x_j} + 2 \frac{\mu}{\mu_t} \frac{k}{y^2} \right] e^{-0.00375 Re_y^2}$$

Table 1

Coefficients for the k- ε turbulence model

C_μ	σ_k	σ_ε	$C_{\varepsilon 1}$	$C_{\varepsilon 2}$	$C_{\varepsilon 4}$
0.09	0.75	1.15	1.15	1.9	-0.33

A complete description of the k- ε model can be found in [13].

6.2 V2F model

The k equation in the V2F model is as for the standard k- ε model, the ε equation is

$$\frac{\partial}{\partial x_j} \left[\rho \bar{u}_j \varepsilon - \left(\mu + \frac{\mu_t}{\sigma_\varepsilon} \right) \frac{\partial \varepsilon}{\partial x_j} \right] = \frac{C_{\varepsilon 1}^Z}{T_s} \left[\mu_t \left(2S_{ij} \frac{\partial \bar{u}_i}{\partial x_j} \right) \right] - \frac{C_{\varepsilon 2}}{T_s} \rho \varepsilon$$

The v^2 equation is

$$\frac{\partial}{\partial x_j} \left[\rho \bar{u}_j v^2 - \left(\mu + \frac{\mu_t}{\sigma_k} \right) \frac{\partial v^2}{\partial x_j} \right] = \rho k f_{22} - 6 \rho v^2 \frac{\varepsilon}{k}$$

The f_{22} equation is

$$L^2 \nabla^2 f_{22} - f_{22} = \frac{1 - C_1}{T_s} \left(\frac{2}{3} - \frac{v^2}{k} \right) - C_2 \frac{\mu_t 2S_{ij} \frac{\partial \bar{u}_i}{\partial x_j}}{\rho k} - 5 \frac{v^2/k}{T_s}$$

With

$$L = C_L \sqrt{\max \left(\frac{k^3}{\varepsilon^2}, C_\eta^2 \left(\frac{v^3}{\varepsilon} \right)^{1/2} \right)}$$

$$T_s = \max \left[\frac{k}{\varepsilon}, C_{kT} \left(\frac{v}{\varepsilon} \right)^{1/2} \right]$$

$$\mu_t = \rho C_\mu v^2 T_s$$

$$C_{\varepsilon 1}^Z = 1 + 0.045 \sqrt{k/v^2}$$

Table 2
Coefficients for the V2F turbulence model

C_μ	σ_k	σ_ε	$C_{\varepsilon 1}$	$C_{\varepsilon 2}$	C_1	C_2	C_L	C_η	C_{kT}
0.22	1.0	1.3	1.4	1.9	1.4	0.3	0.23	70.0	6.0

6.3 LES

After filtering, the Navier-Stokes equations for the LES model are:

$$\frac{\partial \bar{u}_i}{\partial t} + \bar{u}_j \frac{\partial \bar{u}_i}{\partial x_j} = -\frac{1}{\rho} \frac{\partial \bar{p}}{\partial x_i} + \frac{\partial \tau_{ij}}{\partial x_j}$$

The convection term filtered out in the previous equation needs to be model. This is done with the sub-grid scales (SGS) stresses

$$\tau_{ij} = \bar{u}_i \bar{u}_j - \overline{u_i u_j}$$

The Smagorinsky model defines

$$\tau_{ij} - \frac{1}{3} \tau_{kk} \delta_{ij} = 2C_{s2} \Delta^2 |\bar{S}| S_{ij}$$

with

$$\bar{S} = \sqrt{2S_{ij}S_{ij}}$$

where $\Delta = \text{cell volume}^{1/3}$ and C_{s2} is 0.165^2 . The equations for k and ε in the sub-grid model are

$$k_{SGS} = 2C_I \Delta^2 \bar{S}^2$$

with C_I is set to 0.202.

6.4 DES with standard k - ε

The switch between the LED and the RANS mode is done through the length scale

$$\tilde{l} = \min\left(\frac{k^{3/2}}{\varepsilon}, C_{DES} \max(\Delta_x, \Delta_y, \Delta_z)\right)$$

with Δ_x representing the cell size.

PAPER

ON THE NUMERICAL MODELING OF IMPINGING JET HEAT TRANSFER

Mirko Bovo^{1,2}, Sassan Etemad² and Lars Davidson¹

¹ Dept. of Applied Mechanics, Chalmers University of Technology, Gothenburg, Sweden

² Powertrain Analysis, Volvo Car Corporation, Gothenburg, Sweden

ABSTRACT. Steady state numerical simulation of impinging jet heat transfer at $H/D = 2$ is methodically investigated for the following parameters: Turbulence models ($k-\epsilon$ low Re, $k-\omega$ low Re and V2F), grid density (0.25E06, 0.5E06, 1E06 and 2E06 cells), grid topology (2 types), inlet velocity corresponding to Re (10000, 20000 and 30000) and inlet velocity profile (uniform flow and fully developed flow). Effect of numerical discretization scheme is also investigated. The study resulted in 95 simulations. The simulation results are compared with different published experimental data. It was found that the V2F turbulence model performs best for these types of simulations. Furthermore, the choice of turbulence model and inlet velocity profile significantly affects the results. Grid topology is also found to be important. Careful CFD simulations are capable of predicting the heat transfer of impinging jets with good accuracy. (This work can be seen as a best practice guide for this type of simulations).

INTRODUCTION

When fuel is sprayed in the combustion chamber of a reciprocating internal combustion engine, the resulting flow impinging on the cylinder wall presents jet like features. In this case many physical phenomena occur simultaneously. The spray brakes up, evaporates, ignites, burns and eventually meets the cylinder wall as a jet like-flame. Moreover, the whole process is transient (cyclic). Due to its inherent characteristics, the spray combustion process is difficult to measure and to model numerically. Meanwhile, due to the desire for more efficient engines, there is a growing need for a better understanding of the physics in the engine combustion chamber.

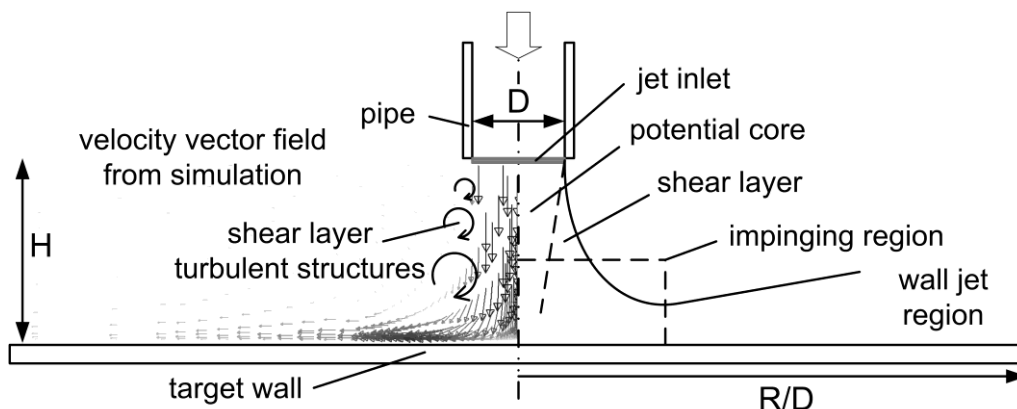


Figure 1. Impinging jet qualitative region definition (right). Impinging jet flow field (left)

Beside internal combustion engines, cases involving heat transfer due to impinging jets are common in industry. This type of flow has among the highest levels of Nusselt number (Nu) known for single

phase flows. Impinging jets are used where high rates of heat transfer are needed, for example in the cooling of electronic devices or turbine blades.

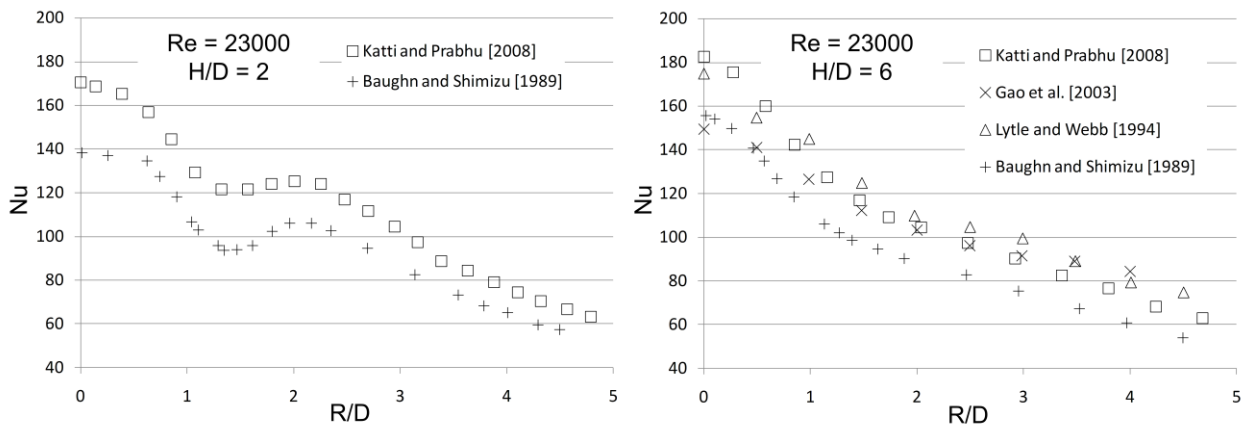


Figure 2. Published experimental results of $Nu(R/D)$. In the left figure, data from Baughn and Shimizu [1989] at $H/D = 2$ and $Re = 23750$ are scaled to $Re = 23000$ using correlations proposed by Katti and Prabhu [2008]

Impinging jet heat transfer depends on several parameters, for example jet Re , nozzle shape, nozzle diameter (D) and nozzle-wall distance (H). For relatively high Re and small H/D (e.g. $Re = 23000$ and $H/D = 2$) the local Nusselt number variation in radial direction $Nu(R/D)$ presents a secondary peak as shown in Figure 2 (left). This phenomenon is not fully understood despite considerable experimental, analytical and numerical efforts [e.g. Gao, et al. 2003, 2006, O'Donovan and Murray 2007]. Various possible explanations are suggested to explain the characteristic secondary peak:

- The flow accelerates in radial direction exiting the impingement zone. High velocity is associated with high heat transfer.
- The boundary layer develops from the stagnation point becoming turbulent and locally increasing the heat transfer rate.
- Turbulent structures grow in the shear layer of the jet (see Figure 1). These structures travel in the jet direction and impact on the target surface in a ring around the impingement point. Resulting velocity fluctuations normal to the wall increase the heat transfer.

Most likely, the interaction of all the presented reasons is the cause of the observed phenomena.

Flow measurements are not trivial. Several authors have published experimental results using different optical measuring techniques. Figure 2 (right) shows measurements of $Nu(R/D)$ from four different authors. Statistical analysis of the data shows an average spreading of about 10% from the mean value.

In CFD, new turbulence models are applied to generic, well documented cases to evaluate their performance. Often the models are tested in simplified conditions, for example 2D cases with symmetric boundary conditions. However, there is a risk that well performing models in such conditions will fail to work for real industrial applications, due to stability problems and poor robustness. Furthermore, even if a model fails to accurately predict absolute values, it might, however, be able to predict trends correctly, which is certainly of great industrial interest. Therefore, robust models such as the $k-\epsilon$ are still widely used in industry.

Impinging jets are notoriously difficult to model in CFD. The flow features of the near wall region are difficult to capture with the common near wall assumptions implemented in the models. Moreover, the flow field presents strong curvatures, unsteadiness and strong pressure strain stresses. The combination of these features makes it difficult to accurately predict the impinging jet flow and consequently its associated convective heat transfer.

This work has the purpose of evaluating the state of the art of the steady state CFD models with complete circular grid for an impinging jet at $H/D = 2$. The influences of several variables are systematically studied using the factorial design of experiment approach. The variables investigated are: Turbulence models (low Re $k-\epsilon$, low Re $k-\omega$, V2F), grid density (0.25E06, 0.5E06, 1E06 cells), grid topology (2 types) and Re_D (10000, 20000, 30000). The calculated Nusselt number is compared with available experimental data. In addition, further simulations are carried out for a selected subset of parameters to investigate the effect of inlet velocity profile (uniform flow and fully developed) and grid density (0.25E06, 0.5E06, 1E06 and 2E06 cells). The study includes a total of 95 simulations.

MODELING METHODOLOGY

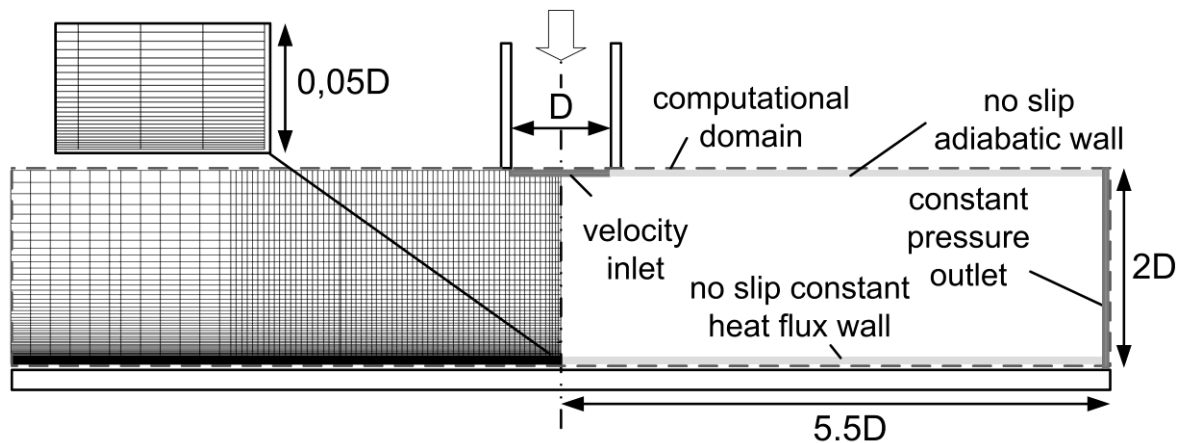


Figure 3. Computational domain and spatial discretization grid in axial direction

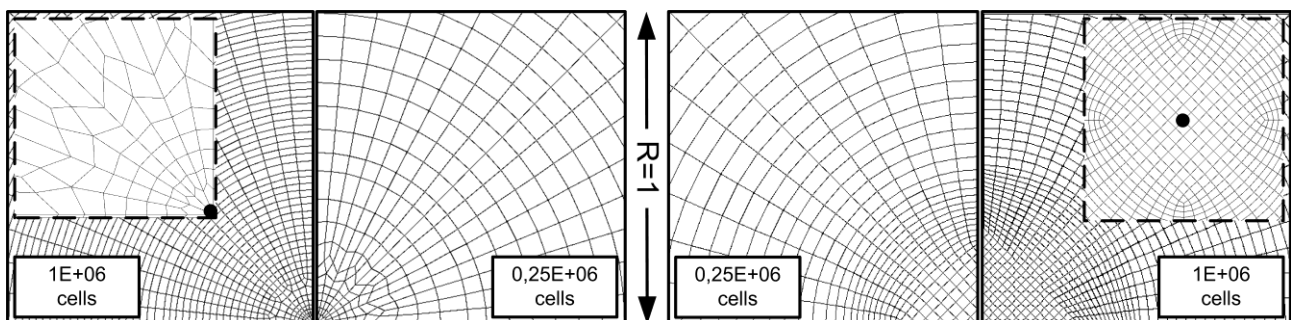


Figure 4. Peacock (left) and Butterfly (right) grid topology. Note that butterfly topology allows only for radial cell density growth while the peacock includes also angular growth. The black dot in the zoomed images represents the grid center.

Computational domain The computational domain is shown in Figure 3. All geometrical dimensions are normalized with the inlet diameter D . The computational domain extends to a radius of

5.5D and a height of 2D. (The pipe is not included in the simulations). The computational domain is a complete circular region.

Grid The grid cross-section in axial direction is shown in Figure 3. The near wall cell thickness adjacent to the wall satisfies $y^+ < 1$ in the entire domain for all cases. The number of cells in the direction normal to the wall is kept constant for the grid independency study. The features of the two different grid topologies are defined in Figure 4. Both topologies result in fully hexahedral structured grids. The topology called “butterfly” is based on a square outline in the center that is transformed in a circular shape. This topology allows only for refinement in radial direction for a given partition of the inner square. The topology called “peacock” can be adapted to discretize any angle. In addition, it allows for grid refinement in both radial and angular directions.

Boundary conditions In general, boundary conditions are selected to be as close as possible to the experimental conditions. This is not always easy to implement and simplifications need to be made. The boundary conditions used are presented and discussed one by one.

Inlet boundary The Inlet Boundary condition is one of the investigated parameters. The impact of uniform flow (plug flow) and fully developed pipe flow are compared. The inlet profile corresponding to fully developed pipe flow is generated with a separate simulation using the V2F model. An infinitely long pipe is simulated by application of cyclic boundary conditions to a short pipe. The variables resulting from the cyclic simulation are mapped as inlet boundary condition for the impinging jet simulations. The mapped variables are: velocity, turbulent kinetic energy and its dissipation rate.

Outlet Constant pressure is used as outlet boundary condition.

Target wall The target wall is defined as no-slip wall with constant wall heat flux.

Upper boundary The upper non-wall fluid boundary is set to adiabatic no-slip wall and consequently defines a confined jet. However, this is not believed to sensibly affect the results. The differences in heat transfer between confined and unconfined jet for $H/D \geq 2$ are shown to be negligible by Gao and Ewing [2006].

Turbulence model The turbulence models used are: standard low Reynolds number $k-\epsilon$, standard low Reynolds number $k-\omega$ and V2F. These models are hereafter referred to as $k-\epsilon$, $k-\omega$, and V2F. Both $k-\epsilon$ and $k-\omega$ are, so called, two-equation model. They model the turbulence by solving the transport equation for two turbulent quantities, namely k and ϵ or ω . The low Re implementations implies that the boundary layer is resolved to the wall including the viscous sub-layer. This allows for an accurate solution of the flow field close to the wall at the expense of a higher computational cost. The V2F differs from the common two-equations models in that in addition to k and ϵ it solves for two additional quantities, the wall-normal Reynolds stress v^2 and its redistribution function f_{22} . The V2F model requires a fine near wall grid.

The transport equations for the different turbulence models are given below in their steady state incompressible form. The equation for the turbulent kinetic energy, k , is the same for all models as is as follows

$$\frac{\partial}{\partial x_j} \left[\rho u_j k - \left(\mu + \frac{\mu_t}{\sigma_k} \right) \frac{\partial k}{\partial x_j} \right] = \mu_t \left(2S_{ij} \frac{\partial u_i}{\partial x_j} \right) - \rho \epsilon \quad (1)$$

With

$$S_{ij} = \frac{1}{2} \left(\frac{\partial u_i}{\partial x_j} + \frac{\partial u_j}{\partial x_i} \right) \quad (2)$$

$$\mu_t = f_\mu \frac{C_\mu \rho k^2}{\varepsilon} \quad (3)$$

Where the damping function f_μ is defined for each model and $\varepsilon = \beta^* k \omega$ in the k- ω model. The equations for the turbulent dissipation rate ε for the k- ε model is the following

$$\begin{aligned} \frac{\partial}{\partial x_j} \left[\rho u_j \varepsilon - \left(\mu + \frac{\mu_t}{\sigma_\varepsilon} \right) \frac{\partial \varepsilon}{\partial x_j} \right] \\ = C_{\varepsilon 1} \frac{\varepsilon}{k} \left[\mu_t \left(2S_{ij} \frac{\partial u_i}{\partial x_j} + P' \right) \right] + C_{\varepsilon 2} (1 - 0.3e^{-R_t^2}) \rho \frac{\varepsilon^2}{k} + C_{\varepsilon 4} \rho \varepsilon \frac{\partial u_i}{\partial x_i} \end{aligned} \quad (4)$$

With

$$P' = 1.33 [1 - 0.3e^{-R_t^2}] \left[2S_{ij} \frac{\partial u_i}{\partial x_j} + 2 \frac{\mu}{\mu_t} \frac{k}{y^2} \right] e^{-0.00375 Re_y^2} \quad (5)$$

$$f_\mu = [1 - e^{-0.0198 Re_y}] \left(1 + \frac{5.29}{Re_y} \right) \quad (6)$$

$$Re_y = \frac{y \sqrt{k}}{\nu} \quad (7)$$

$$R_t = \frac{k^2}{\nu \varepsilon} \quad (8)$$

Table 1
 Coefficients for the k- ε turbulence model

C_μ	σ_k	σ_ε	$C_{\varepsilon 1}$	$C_{\varepsilon 2}$	$C_{\varepsilon 4}$
0.09	0.75	1.15	1.15	1.9	-0.33

A complete description of the k- ε model can be found in Lien, et al. [1996]. A similar implementation is developed for the specific turbulence dissipation rate, ω , in the k- ω model and can be found in Wilcox [1998]. The transport equation for ε in the V2F model is

$$\frac{\partial}{\partial x_j} \left[\rho u_j \varepsilon - \left(\mu + \frac{\mu_t}{\sigma_\varepsilon} \right) \frac{\partial \varepsilon}{\partial x_j} \right] = \frac{C_{\varepsilon 1}^Z}{T_s} \left[\mu_t \left(2S_{ij} \frac{\partial u_i}{\partial x_j} \right) \right] - \frac{C_{\varepsilon 2}}{T_s} \rho \varepsilon \quad (9)$$

The v^2 equation is

$$\frac{\partial}{\partial x_j} \left[\rho u_j \overline{v^2} - \left(\mu + \frac{\mu_t}{\sigma_k} \right) \frac{\partial \overline{v^2}}{\partial x_j} \right] = \rho k f_{22} - 6 \rho \overline{v^2} \frac{\varepsilon}{k} \quad (10)$$

The f_{22} equation is

$$L^2 \nabla^2 f_{22} - f_{22} = \frac{1 - C_1}{T_s} \left(\frac{2}{3} - \frac{\overline{v^2}}{k} \right) - C_2 \frac{\mu_t 2 S_{ij} \frac{\partial u_i}{\partial x_j}}{\rho k} - 5 \frac{\overline{v^2}/k}{T_s} \quad (11)$$

With

$$L = C_L \sqrt{\max \left(\frac{k^3}{\varepsilon^2}, C_\eta^2 \left(\frac{v^3}{\varepsilon} \right)^{1/2} \right)} \quad (12)$$

$$T_s = \max \left[\frac{k}{\varepsilon}, C_{kT} \left(\frac{v}{\varepsilon} \right)^{1/2} \right] \quad (13)$$

$$\mu_t = \rho C_\mu \overline{v^2} T_s \quad (14)$$

$$C_{\varepsilon_1}^z = 1 + 0.045 \sqrt{k/\overline{v^2}} \quad (15)$$

Table 2
 Coefficients for the V2F turbulence model

C_μ	σ_k	σ_ε	$C_{\varepsilon 1}$	$C_{\varepsilon 2}$	C_1	C_2	C_L	C_η	C_{kT}
0.22	1.0	1.3	1.4	1.9	1.4	0.3	0.23	70.0	6.0

Notably, no damping function is used in the V2F model. A complete description of the V2F model and the values for the coefficients can be found in Durbin [1995].

Medium Air is used as fluid, it is simulated as incompressible since the $Ma \ll 0.3$ in the entire domain.

Solver Equations for conservation of mass, momentum, energy and turbulent quantities are solved using the Navier-Stokes solver Star-CD V4.

Convergence strategy Every simulation is initialized with a zero velocity field and run with first (1st) order upwind discretization scheme. The simulations are allowed to run for a maximum of 4000 iterations. The convergence criterion is set to 1E-03 for all monitored residuals. 1st order converged simulations are restarted with the second (2nd) order discretization scheme ‘‘MARS’’ with 0.5 blending factor for the momentum, pressure and temperature equations. These simulations are run for a maximum of 4000 iterations. This strategy is used to help convergence and allows for comparison between results obtained with 1st and 2nd order discretization schemes. The maximum run time for a simulation with such convergence strategy is about 12h on 4 parallel compute nodes equipped with dual Intel Xeon X5460 (Quad-core, 3.16GHz).

RESULTS AND DISCUSSION

The simulations generate a large amount of results to evaluate. These are mainly summarized in diagrams, pictures and graphs. The results are discussed below addressing the different parameters investigated. The first group of 54 simulations is run to allow cross evaluation of 5 different parameters (turbulence model, grid density, grid topology, numerical discretization, Re). Depending on the results a second, less extensive group of simulations is run to further investigate the grid density and the inlet velocity profile effects.

Turbulence model Figure 5 illustrates how the choice of turbulence model impacts the results. It was found that the turbulence model is the most influencing parameter.

$k-\epsilon$ From Figure 5 it is visible that $k-\epsilon$ consistently over-predicts the heat transfer in the stagnation zone. It performs often well for $R/D > 2$ but its performance is inconsistent in this region where it occasionally under-predicts the experimental results significantly. No particular cause is found to explain this deviation.

$k-\omega$ Figure 6 shows that $k-\omega$ is the most successful model in converging with a 2nd order discretization scheme. $k-\omega$ gives consistently good agreement with experiments for small R/D (< 1.5) but deviates for greater R/D (see Figure 5). The spreading effect for $R/D > 4$ is possibly due to the outlet boundary and is common for all models.

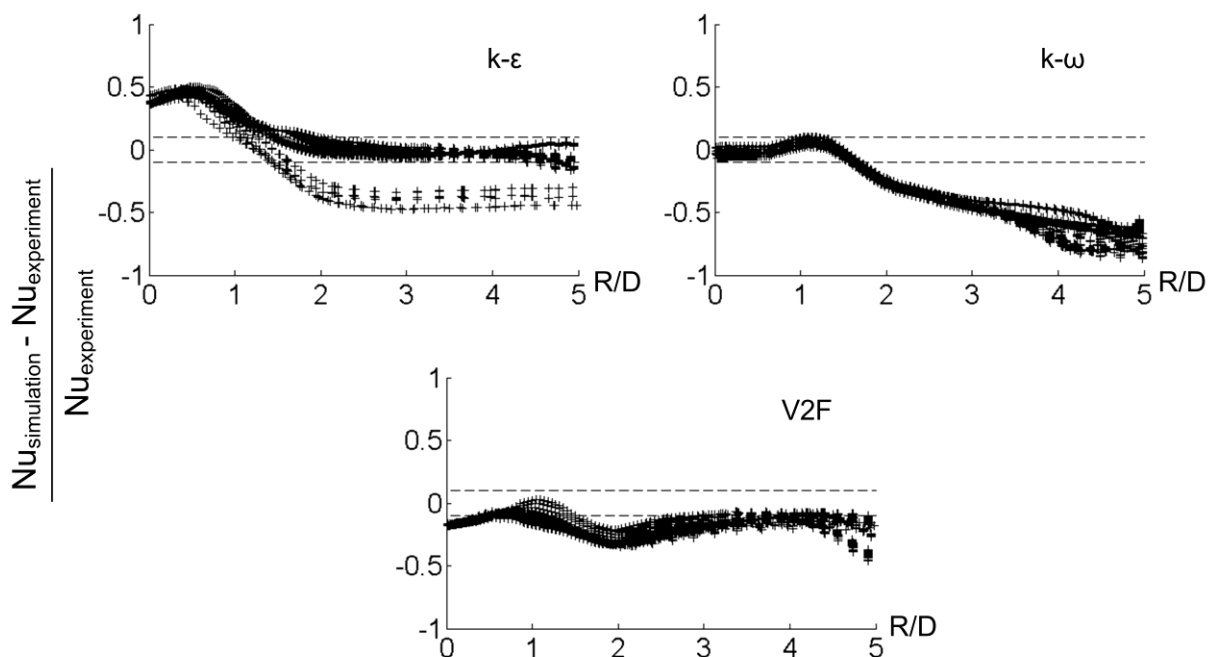


Figure 5. Simulation results for $Re = 20000$ compared with linear interpolation of experimental results from Baughn and Shimizu [1989] and Katti and Prabhu [2008]. Available data from Baughn and Shimizu [1989] are scaled as in Figure 2. All converged simulations are displayed (9 for $k-\epsilon$, 12 for $k-\omega$, 7 for V2F). For each simulation all wall cell values are displayed. The +/-0.1 stripe represents 10% deviation from the average of the two experimental sets

V2F V2F seems to be insensitive to all other parameters (discretization scheme, grid density and topology) as can be seen in Figure 5. It displays a more constant offset from the experimental data for all R/D , somehow under-estimating the experimental results. The spreading in the range $1 < R/D < 2$ occurs for simulations with fine grid and 2nd order discretization scheme. This spreading derives from the fact that the solution is not fully axisymmetric. It is believed that transient phenomena are the cause of this effect. Figure 6 shows that the V2F model reaches convergence with 2nd order discretization scheme only for a few cases, however, the net average difference in Nu between solution obtained with 1st and 2nd order discretization scheme for this model is below 3.3%. This gives confidence on the successfulness of V2F. In other words, better a solution obtained with the V2F model and 1st order discretization scheme converged than one obtained using the $k-\omega$ model with a 2nd order discretization scheme.

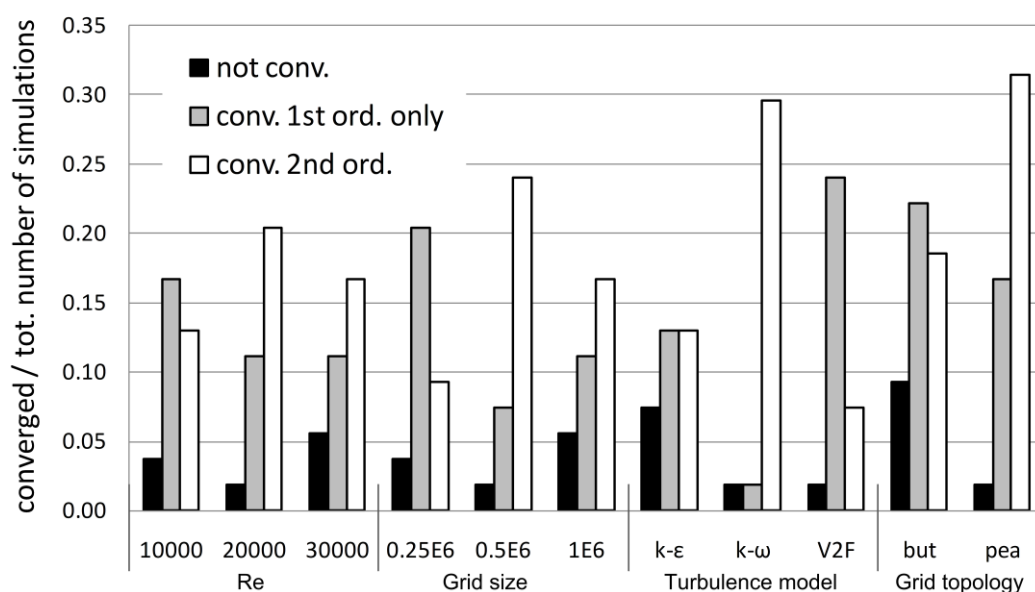


Figure 6. Convergence success relative to parameter. From left Re, grid size, turbulence model and grid topology (but = butterfly and pea = peacock)

Grid size A peak in convergence successfulness is reported for a grid size of $0.5E+06$ cells (see Figure 6). A possible explanation is coarser grids are unable to resolve the flow features correctly. Finer grids, on the other hand, fail to converge to a steady solution because of the existing transient phenomena. Moreover, finer grids generally need more iterations to converge. However, for consistency, all simulations were limited to 4000 iterations in this study.

Numerical discretization scheme Out of 54 simulations, 47 (87%) converged using the 1st order numerical discretization scheme, among these, 27 (50%) converged also using the 2nd order scheme. In Figure 6 is shown the convergence relative to the parameters (Re, grid density, turbulence model, and grid topology). In general, the residuals plot for the non-converged simulations showed a stable cyclic fluctuation. This effect is characteristic of CFD simulations dominated by transient phenomena.

The net average difference in Nusselt number between 1st and 2nd order discretization scheme is 3.8% for the $k-\epsilon$ model, 3% for the $k-\omega$ model and 3.3% for the V2F model. Solutions using a 2nd order scheme are more accurate than 1st order ones and are recommended. However, 1st order discretization

scheme can still be considered physically representative and be used if 2nd order discretization scheme are difficult to obtain. This is recommended if the user has already found confidence in the model.

Grid topology Figure 6 shows that the grid topology called “peacock” is sensibly more successful than the one called “butterfly” in reaching a converged solution with a 2nd order discretization scheme. Further analysis indicates that, in average, peacock grids give closer results to the experimental data. Peacock topology offers more flexibility than butterfly topology. Indeed it allows for spatial refinement in both radial and angular directions. Moreover, peacock grid strategy can be used to discretize partial-circles of arbitrary angles (see Figure 4).

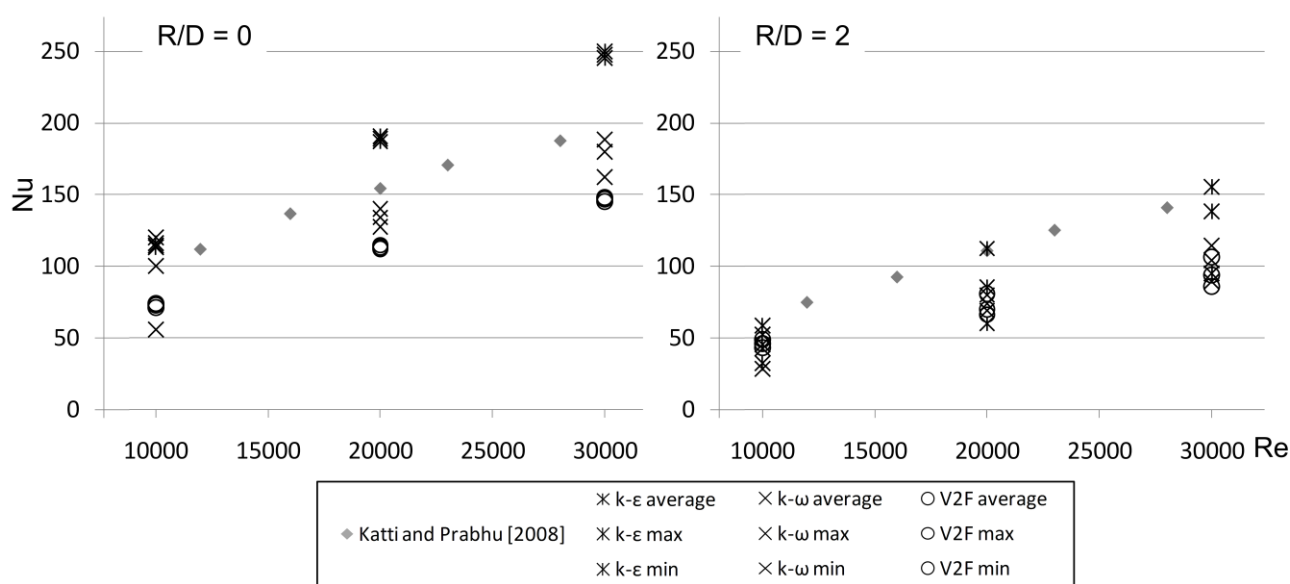


Figure 7. Effect of Re on the Nu at R/D=0 (stagnation point) and R/D = 2. Experimental data from Katti and Prabhu [2008]. For each turbulence model 3 values are presented: average, maximum and minimum. Note that their difference might be within graphical resolution (i.e. they overlap)

Effect of Reynolds Number For impinging jets the heat transfer is a strongly dependent on the Reynolds number. Figure 7 compares simulation results with experimental data for various Re at two different locations. Although the absolute values do not agree with the measured data, the main trend for Nu as function of Re at R/D = 0 is captured by all turbulence models. At higher R/D, results for the k-ε show a wide spreading deriving from its stronger dependency on other parameters. k-ω and V2F present a more consistent offset from the experimental data. These features support the results presented in Figure 5 which refer only to Re = 20000.

Grid independency study The selected group of cases used for the grid independency study is defined by the following parameters: Re =20000, k-ε and V2F, butterfly and peacock grid topology, grid density (0.25E06, 0.5E06, 1E06 and 2E06 cells). In general, no significant differences are found between the results obtained for grids with more than 0.5 E+06 cells. k-ε presents significant difference between results obtained with 0.25 E+06 and 0.5E+06 cells. V2F presents only minor differences between all the grids tested. This indicates that the degree of grid dependency varies with turbulence model.

Effect of inlet velocity profile The experimental data used for comparison in this work come from experiments performed with jets deriving from a fully developed pipe flow, while all simulations presented above are performed with uniform flow. Impinging jet heat transfer is a strong function of the Reynolds number as can be seen in Figure 7. Re is directly related to the flow momentum. A fully developed velocity profile has a higher flow momentum in the pipe centre compared to the corresponding uniform flow (i.e. for the same Re). This affects the impinging jet heat transfer.

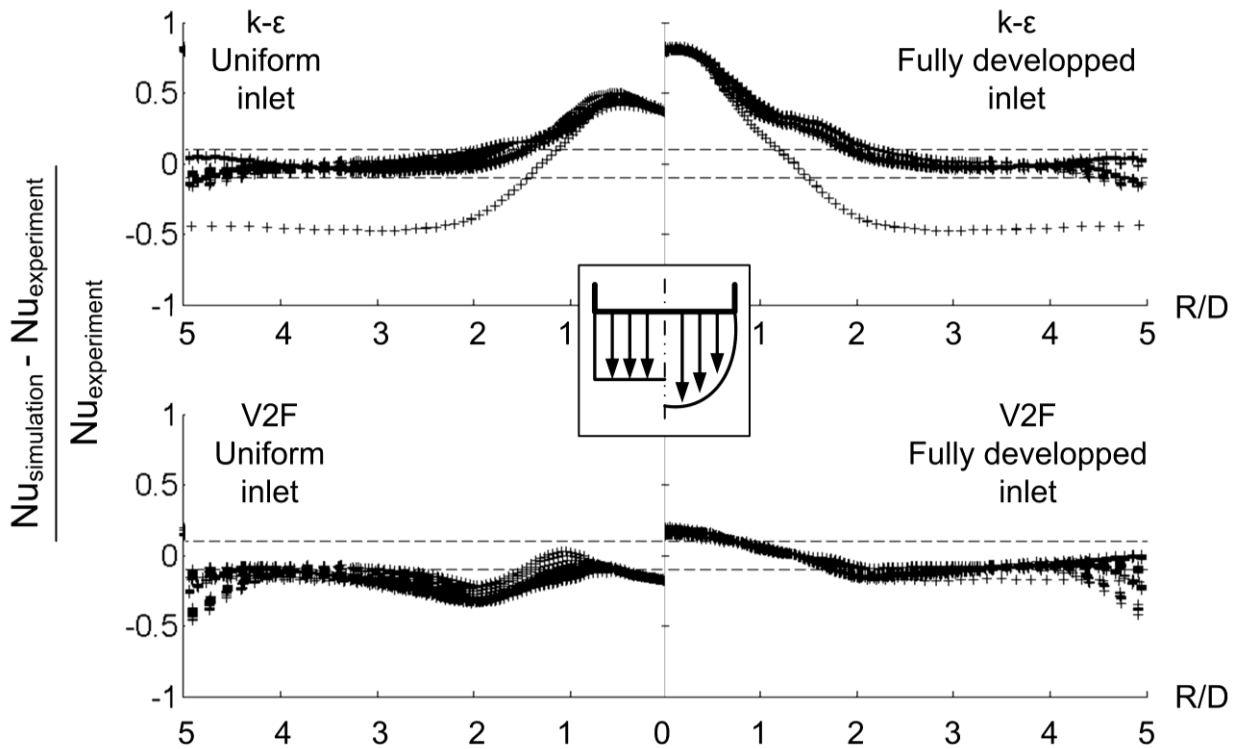


Figure 8. Effect of inlet velocity profile. Simulation results for $Re = 20000$, grid density $0.5E+06$ and $1E+06$, butterfly and peacock grid topology. Comparison with linear interpolation of experimental results from Baughn and Shimizu [1989] and Katti and Prabhu [2008]. Available data from Baughn and Shimizu [1989] are scaled as in Figure 2. For each simulation all wall cell values are displayed. The ± 0.1 stripe represents 10% deviation from the experimental results interpolation according with statistical analysis

Simulations are run to study the effect of inlet velocity profile with the following parameters: $Re = 20000$, $k-\epsilon$ and V2F turbulence models, butterfly and peacock grid topology, $0.5E+06$ and $1E+06$ grid density. The applied velocity profile is obtained as described in the “modeling methodology” section. The velocity at the pipe center for the fully developed profile is about 1.23 times the velocity of a uniform flow profile (at $Re = 20000$). Notably, the turbulent kinetic energy from the simulation is about twice the one used for the simulations with uniform flow inlet.

Results regarding the effect of the inlet velocity boundary profile are presented in Figure 8. The results obtained with V2F and fully developed inlet velocity profile agree with the experimental results almost within the estimated confidence of the experimental data.

For $R/D < 2$ the effect of the velocity profile is very important as shown in Figure 8. For greater R/D the influence of the inlet conditions are negligible for $k-\epsilon$ while some effects are still noticeable for the simulations performed with V2F.

Flow field and heat transfer distribution The comparison between simulation results and the experimental data showed good agreement for V2F. Results obtained with this model are used to get an insight of the flow field and its correlation to the heat transfer phenomena.

In Figure 9 the velocity field is compared for uniform and fully developed inlet flow. With the fully developed flow the jet has a considerably higher core velocity which is retained farther downstream the nozzle. Consequently, the jet is more compact and concentrates its effects on a smaller surface. As a result the heat transfer in the impingement zone is increased as can be seen in Figure 10.

The wall jet region is fed by the free stream jet. In the case with fully developed flow, the wall jet is fed within a smaller area, this can be clearly noticed through the difference in shape between the two cases in the inflection zone ($R/D = 0.5$, $H/D = 0.25$ in Figure 9). The result is a higher mass flow rate per unit cross section in the wall jet region, the flow is hence forced to a stronger acceleration, developing a higher velocity closer to the impingement point. The difference in the flow field is clear when analyzing the boundary layer velocity profile (bottom pictures in Figure 9). The flow field has a direct influence the heat transfer. The consequences of the flow field difference can be seen in Figure 10. The locations and the magnitude of the secondary peaks for $Nu(R/D)$ are sensibly different for the two cases presented. The results obtained with the fully developed inlet velocity match the experimental results quite well, including the location and magnitude of the secondary peak.

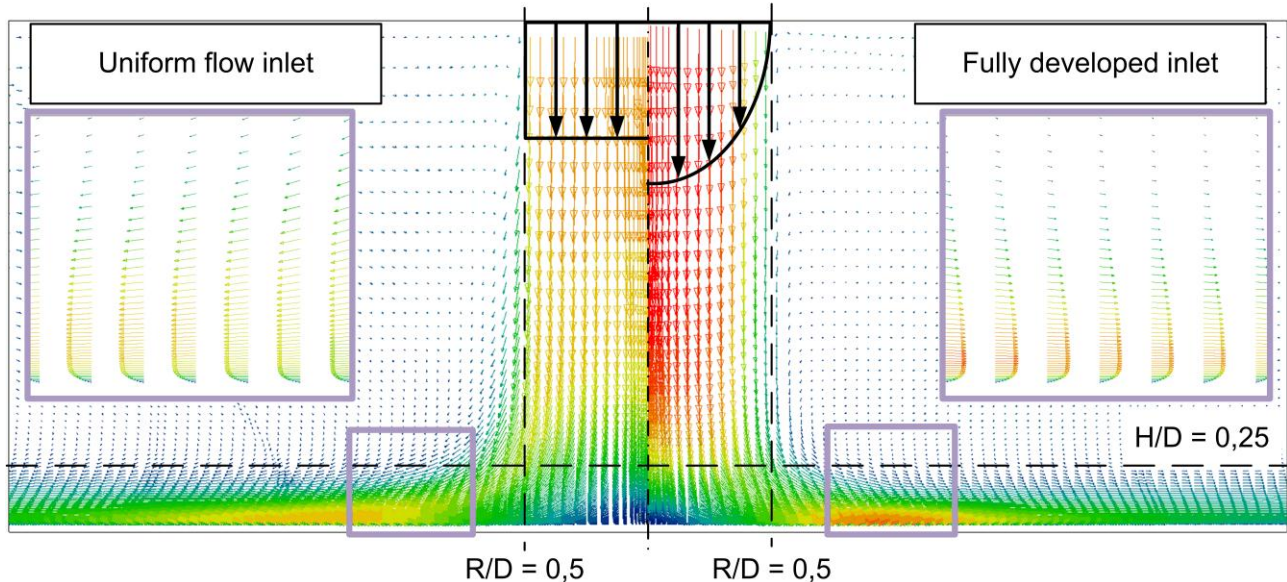


Figure 9. Comparison between uniform and fully developed inlet velocity profiles (qualitative illustration). Numerical simulation parameters ($Re = 20000$, V2F turbulence model, $0.5E+06$ grid cells, peacock topology, 2^{nd} order discretization scheme).

Data from all wall cells are plotted in Figure 10. The data scatter implies that the numerical solution is not perfectly axisymmetric. The data spreading is highest in the secondary peak area. Important transient phenomena are expected in this area where toroidal vortices created in the shear layer impact the target wall. Moreover, this study shows a relatively low convergence success (about 50%

considering all simulations performed). These results suggest that a representative axisymmetric steady state solution is difficult to achieve and a transient simulation approach might give considerably better results.

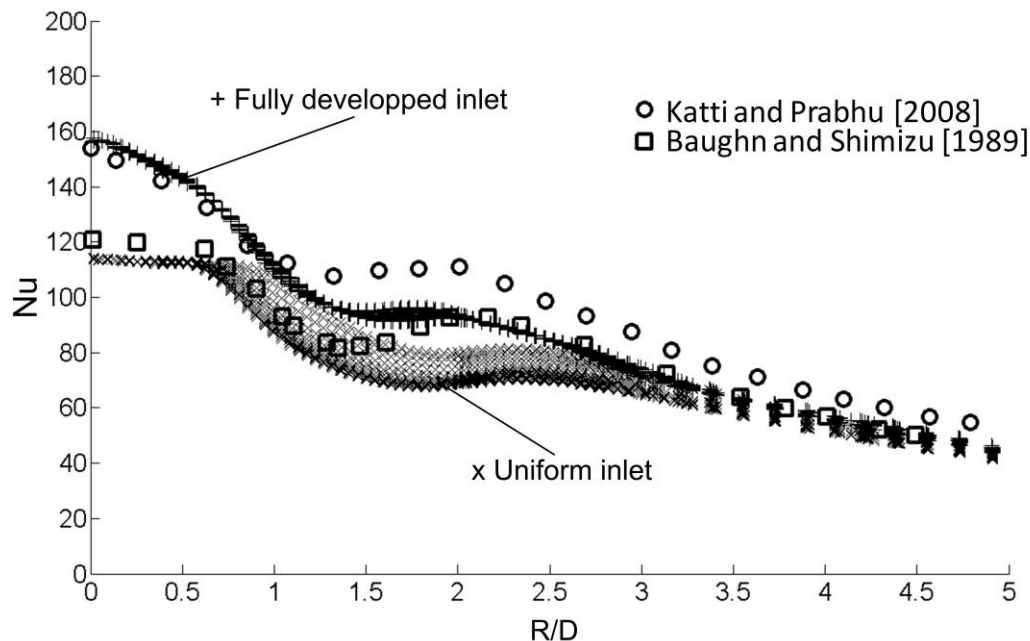


Figure 10. $Nu(R/D)$ comparison between results with the V2F model and experiments at $Re = 20000$. Numerical simulation parameters ($Re = 20000$, V2F turbulence model, $0.5E+06$ grid cells, peacock topology, 2nd order discretization scheme). Available data from Baughn and Shimizu [1989] are scaled as in Figure 2

CONCLUSIONS

The present work can be seen as a best practice guide for steady CFD state modeling of impinging jets at $H/D=2$. As turbulence model V2F performs best. The peacock grid topology gives the best results both with respect to convergence robustness and accuracy in results. Finer grids give better results but show more often convergence problems. 2nd order numerical discretization gives slightly closer results to the experimental data than 1st order but encounters more often convergence problems. For all cases the choice of turbulence model has a much stronger influence on the results than the other variables (e.g. discretization order or grid density). Moreover, it is shown how grid independency is affected by the turbulence model. The inlet velocity profile has a significant influence on the simulation results. Uniform velocity profile cannot be used to represent fully developed velocity profile in these types of flows.

CFD simulation can be used to predict impinging jet heat transfer with accuracy close to experimental confidence. However, the task is not straight forward and careful model set up is necessary.

Two facts imply that important transient behavior prevent the simulation from reaching a converged steady state solution.

- The use of finer grid and higher numerical discretization order more often leads to non axisymmetric solutions but better agreement with the experimental data.
- The relatively low convergence success due to the cyclic oscillation of the residuals.

Significant transient phenomena are also measured by O'Donovan and Murray [2007] and pointed out as explanation for the peculiarity of impinging jet flows. It appears that impinging jets are very time-dependent and steady state simulations are inherently not capable of representing the physics correctly. If a higher precision is required a transient simulation approach should be considered instead of attempting steady state simulation with higher resolution (e.g. higher grid density).

REFERENCES

- Baughn, J. W. and Shimizu S. [1989], Heat transfer measurements from a surface with uniform heat flux and an impinging jet, *ASME J. Heat Transfer* 111 1097.
- Durbin, P.A. [1995], Separated flow computations with the $k-\epsilon-v^2$ model, *AIAA Journal*, 33(4), 659-664
- Gao, N., Sun H. and D. Ewing [2003], Heat transfer to impinging round jets with triangular tabs, *Int. J. Heat Mass Transfer* 46 2557–2569.
- Gao N. and Ewing D. [2006], Investigation of the effect of confinement on the heat transfer to round impinging jets exiting a long pipe, *Int. J. of Heat and Fluid Flow* 27 33–41.
- Lytle, D. and Webb B.W. [1994], Jet impingement heat transfer at low nozzle plate spacings, *Int. J. Heat Mass Transfer* 37 1687–1697.
- Lien, F.S., Chen, W.L. and Leschziner, M.A. [1996], Low-Reynolds-Number Eddy-Viscosity Modelling Based on Non-linear Stress-Strain/Vorticity Relations, *Proc. 3rd Symp. on Engineering Turbulence Modelling and Measurements*, Crete, Greece.
- Katti, V. and Prabhu S.V. [2008], Experimental study and theoretical analysis of local heat transfer distribution between smooth flat surface and impinging air jet from a circular straight pipe nozzle, *Int. J. Heat Mass Transfer* 51 4480–4495.
- O'Donovan T. S. and Murray D. B. [2007], Jet impingement heat transfer – Part I: Mean and root-mean-square heat transfer and velocity distributions, *Int. J. Heat and Mass Transfer* 50 3302–3314.
- Wilcox, D.C. [1998], *Turbulence modelling for CFD*, 2nd edition, DCW Industries, Inc.